

Arrayed single-gene perturbations identify drivers of human anterior neural tube closure

Roya E Huang^{1,2,3*†}, Giridhar M Anand^{1,2,3*†}, Heitor C Megale^{1,2,3}, Jason Chen^{1,3}, Chudi Abraham-Igwe³, Sharad Ramanathan^{1,2,3*}

¹Department of Stem Cell and Regenerative Biology, Harvard University, Cambridge, United States; ²School of Engineering and Applied Sciences, Harvard University, Cambridge, United States; ³Department of Molecular and Cellular Biology, Harvard University, Cambridge, United States

eLife Assessment

This **landmark** study investigates how patterned human gastruloids can provide insights into neural tube closure. Using a screen, they identified positive and negative regulators and defines the epistasis among them using optimization of micro-pattern based gastruloid protocol and CRISPRi. This technical tour de force is **exceptional** and one of the first studies to reveal new knowledge on human development through embryo models.

*For correspondence:

roya_huang@berkeley.edu (REH);
anandg1@mskcc.org (GMA);
sharad@cgr.harvard.edu (SR)

†These authors contributed equally to this work

Competing interest: See page 21

Funding: See page 21

Preprint posted
22 July 2025

Sent for Review
18 July 2025

Reviewed preprint posted
04 September 2025

Reviewed preprint revised
27 April 2026

Version of Record
07 July 2026

Reviewing Editor: Valerie Horsley, Yale University, United States

© Copyright Huang, Anand et al. This article is distributed under the terms of the [Creative Commons Attribution License](https://creativecommons.org/licenses/by/4.0/), which permits unrestricted use and redistribution provided that the original author and source are credited.

Abstract Genetic studies of human embryonic morphogenesis are constrained by ethical and practical challenges, restricting insights into developmental mechanisms and disorders. Human pluripotent stem cell (hPSC)-derived organoids provide a powerful alternative for the study of embryonic morphogenesis. However, screening for genetic drivers of morphogenesis in vitro has been infeasible due to organoid variability and the high costs of performing scaled tissue-wide single-gene perturbations. By overcoming both these limitations, we developed a platform that integrates reproducible organoid morphogenesis with uniform single-gene perturbations, enabling high-throughput arrayed CRISPR interference screening in hPSC-derived organoids. To demonstrate the power of this platform, we screened 77 transcription factors in an organoid model of anterior neurulation to identify *ZIC2*, *SOX11*, and *ZNF521* as essential regulators of neural tube closure. We discovered that *ZIC2* and *SOX11* are required for closure, while *ZNF521* prevents ectopic closure points. Single-cell transcriptomic analysis of perturbed organoids revealed co-regulated gene targets of *ZIC2* and *SOX11* and an opposing role for *ZNF521*, suggesting that these transcription factors jointly govern a gene regulatory program driving neural tube closure in the anterior forebrain region. Our single-gene perturbation platform enables high-throughput genetic screening of in vitro models of human embryonic morphogenesis.

Introduction

Pioneering genetic screens in model organisms—including notable work in *Drosophila* (Nüsslein-Volhard and Wieschaus, 1980) and zebrafish (Nüsslein-Volhard, 2012)—demonstrate that key regulators of embryonic morphology and tissue patterning are revealed by organism-wide gene perturbations. Performing analogous screens in human embryos is prohibited for ethical reasons, and screens in mammalian model organisms present significant challenges: generating clonal knockout lines in mice is expensive (Aguilera-Castrejon et al., 2021; Justice and Dhillon, 2016; Skarnes et al.,

eLife digest Proper organ morphology is a critical outcome of embryonic development. However, the genetic basis of human developmental disorders affecting tissue morphogenesis, such as neural tube closure (a process essential for the formation of the brain and spinal cord), has proven difficult to study because of ethical limitations on human embryo research.

Three-dimensional stem cell-derived models of human embryogenesis and organogenesis provide a promising alternative for investigating the genetics of morphogenesis. Nevertheless, high-throughput genetic screens in organoid systems typically rely on ‘pooled perturbation approaches’, in which only a small fraction of cells within each organoid carries a given genetic perturbation. While these methods have advanced our understanding of gene function at the single-cell level, they are not ideal for studying how individual genes regulate multicellular processes such as morphogenesis.

Huang et al. sought to identify genes required for neural tube closure in the developing human forebrain using a stem cell-derived organoid model. The researchers first aimed to establish a more reproducible three-dimensional model of human neural tube closure. They then sought to develop a high-throughput method for targeting individual genes across micropatterned organoids, enabling parallel assessment of gene-specific contributions to neural tube closure.

Huang et al. developed an approach for uniform gene knockdown across entire human pluripotent stem cell (hPSC)-derived organoids. They used this method to identify three transcriptional regulators of neural tube closure in the developing human forebrain. They found that arranging organoids in a hexagonal pattern promoted highly symmetrical breaking of ectodermal tissues, resulting in a reproducible three-dimensional model of human neural tube closure.

They next developed a high-throughput method for targeting single genes broadly and uniformly across each organoid, by generating and applying a high density of lentiviruses carrying gene-editing tools (CRISPRi dual-guide RNAs). This allowed them to examine the roles of individual genes in the tissue-wide process of morphogenesis. Guided by neural gene expression analyses, 77 transcription factor candidates were screened, and three genes (ZIC2, SOX11, and ZNF521) were identified as essential for proper neural tube closure.

The platform developed by Huang et al. is broadly applicable to genetic investigations of morphogenesis in human stem cell-derived models, enabling high-throughput analyses of genes that regulate developmental processes. Future studies could evaluate the roles of ZIC2, SOX11 and ZNF521 in human neural tube defects by assessing their sequence and expression in patients affected by such conditions. In addition, the relationship between these genes and other known genetic contributors to neural tube defects remains an important area for future investigation.

2011) and direct translation to human biology is complicated by species-specific differences in gene regulation, developmental timing, and tissue organization (Xue et al., 2013).

Human pluripotent stem cell (hPSC)-derived organoids offer an attractive alternative for modeling human embryonic morphogenesis in vitro. Advances in three-dimensional differentiation have enabled the generation of increasingly complex organoid models that recapitulate the development of different human tissues (Sanaki-Matsumiya and Kageyama, 2022; Yamanaka et al., 2023; Oldak et al., 2023; Miao et al., 2023; van der Valk et al., 2023; Hofbauer et al., 2021; Corsini and Knoblich, 2022). The growing reproducibility of these models following the incorporation of bioengineering methods (Anand et al., 2023; Hofer and Lutolf, 2021; Karzbrun et al., 2021; Xue et al., 2025; Yaman and Ramanathan, 2023) makes them ideally suited for genetic perturbation screens. Despite progress, it remains challenging to interrogate the effects of genes on morphogenesis at scale. High-throughput screens to understand gene function in organoids have relied on CRISPR/Cas9-based approaches in which organoids are transduced with a pooled lentiviral library, with each virus carrying guide RNAs targeting a distinct gene. The approach produces mosaic organoids where multiple genes are knocked down in distinct cell sub-populations within the same organoid (Esk et al., 2020; Fleck et al., 2023; Li et al., 2023). This degree of mosaicism makes it impossible to study tissue-wide morphogenesis, which occurs via the coordination of genes acting across many cells. Pooled screens are limited to single-cell genomic, epigenomic, or transcriptomic profiling as a readout of gene function, in contrast to morphological phenotypes assessed by classical screens in developmental biology.

The study of morphogenesis at scale *in vitro* requires the ability to knock out or knock down genes individually throughout entire organoids. This typically requires the generation of knockout or knockdown cell lines through clonal analysis, a process that is prohibitive for high-throughput applications due to the cost and labor involved in isolating and expanding correctly edited clones (**Huber et al., 2023; Menche and Farin, 2021; Sun et al., 2021**). The ability to achieve homogeneous gene knockdown across a cell population in a non-clonal manner—using technologies such as CRISPR interference (CRISPRi)—could enable high-throughput morphological screens (**Mandegar et al., 2016**). Lentiviruses carrying CRISPRi guide RNAs offer a means to perform such non-clonal knockdowns, and if delivered with high efficiency, can eliminate the need for clonal purification and expansion. However, this strategy faces several challenges: current protocols to generate high-titer lentivirus rely on laborious and time-consuming concentration steps which are not amenable to high-throughput workflows (**Valcourt et al., 2021**), and it is difficult to achieve high-efficiency lentiviral transduction without associated cell death (**Brown et al., 2020**). Overcoming these critical challenges would enable genetic perturbations at a scale not currently feasible in organoids or mammalian model systems, allowing systematic interrogation of the genes that drive human embryonic morphogenesis.

Here, by developing a method to generate and apply high-titer lentivirus directly to stem cells in parallelized small volumes, we established a high-throughput arrayed CRISPRi platform for uniform knockdown of individual genes across whole hPSC-derived organoids. To demonstrate the utility of this platform, we applied it to study anterior neurulation, a critical morphogenetic event in brain formation in which the flat anterior neural plate bends and fuses to form a closed neural tube (**Smith and Schoenwolf, 1997; Nakatsu et al., 2000**). Defects in anterior neural tube closure cause anencephaly, which is embryonic lethal. This lethality limits genetic linkage and association studies (**Ishida et al., 2018**) and makes anterior neurulation of critical importance to study *in vitro*. To systematically determine genes required for anterior neurulation, we established a robust *in vitro* hPSC-derived anterior neural tube organoid model and used our CRISPRi platform to screen 77 individual candidate genes encoding transcription factors for their contribution to neural tube morphogenesis. We found that *ZIC2* and *SOX11* are required for anterior neural tube closure and co-regulate a gene expression program in opposition to *ZNF521*, which is required to prevent ectopic closure points. These findings show the impact of scalable single-gene perturbations in identifying genes driving morphogenetic processes *in vitro* and have direct implications for understanding the genetic causes of congenital malformations.

Results

A reproducible *in vitro* model of human anterior neurulation

We previously discovered that when spatially arranged hPSC-derived epiblast-like cysts are exposed to posteriorizing signals, they break symmetry and undergo patterning (**Anand et al., 2023; Yaman and Ramanathan, 2023**). Building on this approach, we established an organoid model of human anterior neurulation (**Figure 1A; Virtual Human Embryo, 2026**). Briefly, we seeded hPSCs onto a glass coverslip containing hexagonally arranged 250- μm -diameter micropatterns of extracellular matrix (Matrigel), including a central micropattern (**Figure 1—figure supplement 1A**), with 100 μm edge-to-edge spacing. After allowing hPSCs to form two-dimensional epithelial colonies on micropatterns, we embedded them in concentrated Matrigel, prompting hPSC colonies to fold into three-dimensional epithelial cysts with apicobasal polarity and single lumens. To induce anterior neural and surface ectoderm fates, we inhibited BMP, TGF β , and WNT signaling for 2 days, then added recombinant human BMP4 for 4 days with continued TGF β and WNT inhibition (**Figure 1—figure supplement 1B–D, Methods**) (**Karzbrun et al., 2021; Valcourt et al., 2021; Britton et al., 2019**). Under these signaling conditions, the spatially arranged cysts differentiated into organoids with inward-facing neural ectoderm (NCAD⁺) and outward-facing surface ectoderm (ECAD⁺) (**Figure 1B, C**). Over the course of 4 days of BMP4 exposure, differentiating cysts displayed hallmarks of anterior primary neurulation, including thickening and elevation of the neural plate (Day 2), basal apposition of the neural and surface ectoderm (Day 3), and fusion of the neural folds at the midline to form a closed neural tube with overlying surface ectoderm (Day 4) (**Figure 1B, C, Figure 1—figure supplement 1E, Figure 1—videos 1 and 2**). In replicate experiments, all organoids displayed a closed neural lumen as assayed by a closed ring of apical NCAD on Day 4 (**Figure 1D, Figure 1—figure supplement 1F, N =**

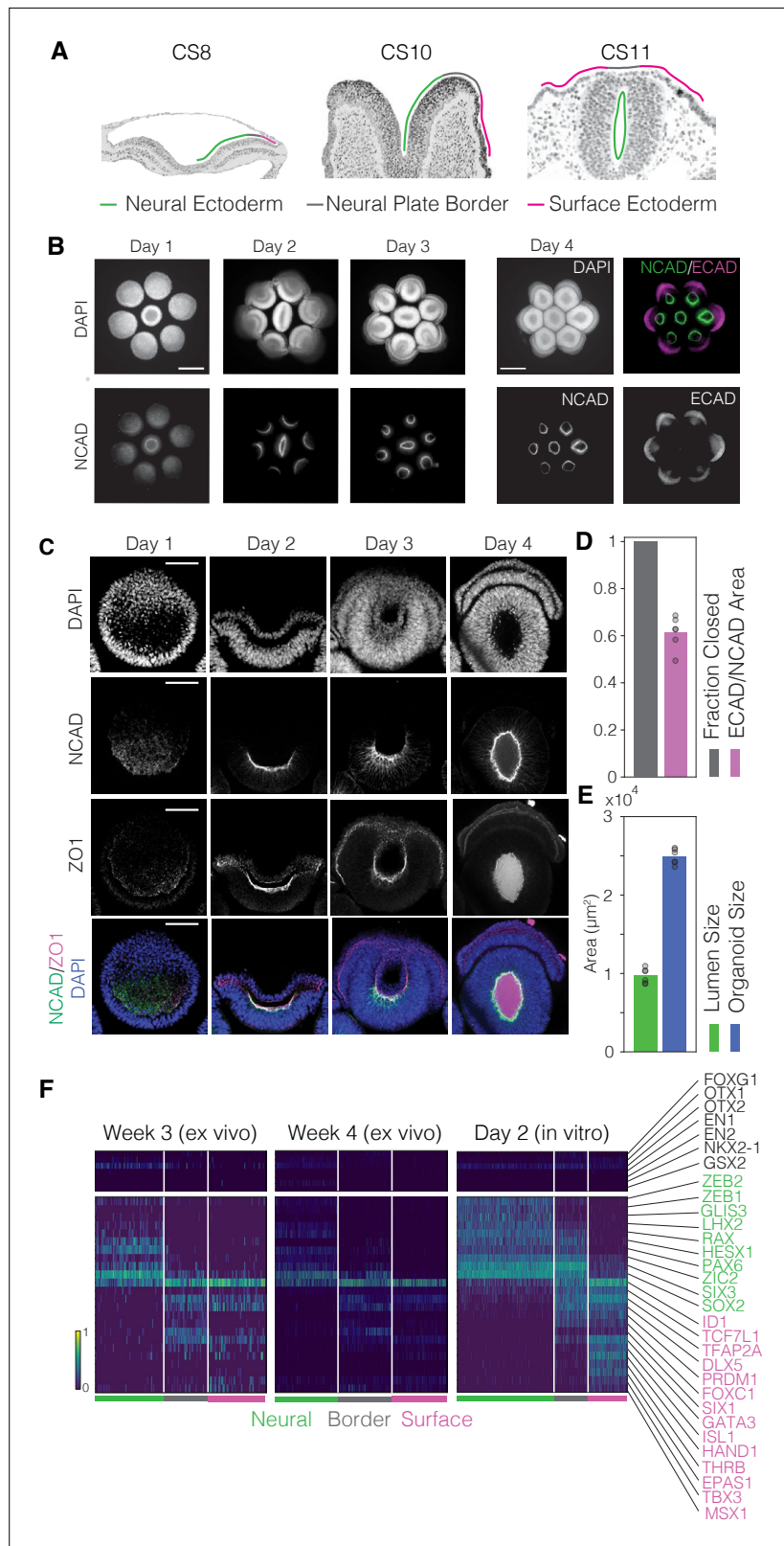


Figure 1. An in vitro model of human anterior neurulation. **(A)** Micrographs of human embryo sections from the Virtual Human Embryo project showing sequential neural plate bending, neural fold elevation, and neural tube closure from Carnegie Stages (CS) 8, 10, and 11. Tissues are outlined according to epithelial thickness, denoting the approximate location of neural ectoderm (green), neural plate border (gray), and surface ectoderm (magenta).

Figure 1 continued on next page

Figure 1 continued

Scale bar: 300 μm . **(B)** Top-down epifluorescence images of seven three-dimensional, hexagonally arranged neural tube organoids 1, 2, and 3 days after BMP4 addition, stained for nuclear marker DAPI and neural ectoderm marker N-cadherin (NCAD). Rightmost set of four images shows the organoids at Day 4 of differentiation, stained for DAPI, NCAD, and surface ectoderm marker E-cadherin (ECAD). The six outer organoids show radial patterning, with inward-facing neural ectoderm (NCAD+, green) and outward-facing surface ectoderm (ECAD+, magenta). Scale bar: 300 μm . **(C)** Top-down confocal images of a representative single outer organoid after exposure to BMP4 for 1, 2, 3, and 4 days, fixed and stained for DAPI, NCAD, epithelial tight junction marker ZO-1. A neural plate is distinguishable by Day 2, which elevates and folds from a 'U' shape to a 'C' shape by Day 3 and finally fuses on Day 4 to enclose a single lumen ('O' shape). Extraneous ZO-1 staining in the lumen on Day 4 is likely due to dead cells that have been shed into the lumen during and after folding (see **Figure 1—videos 1 and 2**). Scale bar: 100 μm . **(D)** Quantification of neural tube closure in Day 4 organoids (left) and relative proportion of ECAD+ surface ectoderm to NCAD+ neural ectoderm (right) as measured by the projected area (see Methods). 100% of the outer organoids across biological replicates ($N = 4$ biological replicates, $n = 24$ organoids) exhibit closure based on observation of a continuous ring of NCAD (**Figure 1—figure supplement 1F**). The ratio of the surface to neural ectoderm has a coefficient of variation (CV) of 0.01. **(E)** Quantification of lumen (left) and organoid size (right) across Day 4 organoids ($n = 6$ organoids), based on the projected area enclosed by NCAD and DAPI staining (Methods). Lumen and organoid size have a CV of 0.09 and 0.04, respectively. **(F)** Hierarchical clustering in the space of genes identified by sparse multimodal decomposition (Methods) of single-cell RNA-sequencing data from Week 3 human embryos, Week 4 human embryos, and organoids on Day 2 after BMP4 addition, showing the existence of neural ectoderm (green), neural plate border (gray), and surface ectoderm (magenta) cell types in vitro and ex vivo marked by similar gene expression patterns. Distinct sets of transcription factors are enriched in neural and surface ectoderm, highlighted in green and magenta, respectively, and a subset of these are co-expressed in border ectoderm. Neural ectoderm cells express high levels of forebrain-associated transcription factors (OTX1, OTX2, LHX2, and SIX3), and low levels of midbrain/hindbrain- (EN1 and EN2) or ventral forebrain- (NKX2-1 and GSX2) associated transcription factors. Gene expression (color bar, bottom left) is normalized to median transcript count, followed by log- and min-max normalization.

The online version of this article includes the following video and figure supplement(s) for figure 1:

Figure supplement 1. Development and validation of a human pluripotent stem cell (hPSC)-derived in vitro model of anterior neurulation.

Figure 1—video 1. Timelapse of actin during neural folding, hours 0–7 after BMP4 addition.
<https://elifesciences.org/articles/108224/figures#fig1video1>

Figure 1—video 2. Timelapse of actin during neural folding, hours 9–33 after BMP4 addition.
<https://elifesciences.org/articles/108224/figures#fig1video2>

4 biological replicates; $n = 24$ organoids). Furthermore, quantification of features including organoid size, lumen size, and ECAD/NCAD area ratio showed that our in vitro organoids were reproducible with respect to tissue patterning and morphogenesis (**Figure 1C, E, Figure 1—figure supplement 1E**, $N = 4$ biological replicates, $n = 24$ organoids).

To characterize the cell types in our organoid model at the onset of neurulation, we performed single-cell RNA-sequencing (scRNA-seq) at Day 2 of BMP4 exposure, when the neural plate begins to elevate. To overcome limitations of existing computational methods in identifying cell types from scRNA-seq data, we applied our previously validated unsupervised dimensionality reduction method, sparse multimodal decomposition (SMD) (**Melton and Ramanathan, 2021**). Using SMD, we identified a set of bimodally expressed genes that separated the cells into three cell types distributed along the mediolateral axis within the ectoderm: neural ectoderm, neural plate border, and surface ectoderm (Methods, **Figure 1F**, left). The three cell types showed a graded expression of *SOX2* in the medial-to-lateral direction: highest in the neural ectoderm, intermediate in the neural plate border, and lowest in the surface ectoderm, consistent with studies in model organisms (**Roellig et al., 2017**). Neural ectoderm cells expressed forebrain-associated transcription factors, including *LHX2*, *HESX1*, *PAX6*, *SIX3*, *ZEB1*, and *ZEB2* (**Debacker et al., 1999; Hermesz et al., 1996; Oliver et al., 1995; Takagi et al., 1998; Van de Putte et al., 2003; Walther and Gruss, 1991; Xu et al., 1993**). Surface ectoderm cells expressed canonical transcription factors, including *TFAP2A* and *GATA3* (**Debacker et al., 1999; Leask et al., 1991**). Meanwhile, the neural plate border population co-expressed neural ectoderm transcription factors *PAX6* and *SIX3* as well as surface ectoderm transcription factors *TFAP2A* and *GATA3*, along with *DLX5* and *SIX1*, which mark cranial placodes arising at the neural plate border

(Laclef et al., 2003; McLaren et al., 2003). Notably, all ectodermal cell types expressed *OTX1* and *OTX2* but not *EN1* or *EN2*, indicating forebrain rather than midbrain/hindbrain identities (Li and Joyner, 2001). Additionally, ventral markers *NKX2-1* and *GSX2* were absent, suggesting a dorsal identity (Corbin et al., 2003). We did not observe neural crest cells, marked by transcription factors *SOX10* and *FOXD3* (Bondurand et al., 1998; Dottori et al., 2001). This is consistent with neural tube closure in the human embryo at the anterior forebrain level, where no neural crest cells are present (O’Rahilly and Müller, 2002). To compare our findings with ex vivo gene expression patterns, we applied the same approach to published scRNA-seq data from 3- to 4-week-old human embryos at the neurula stage (Zeng et al., 2023). Using the same SMD approach, we identified the same three ectodermal cell types ex vivo, with gene expression patterns that matched those observed in our organoids (Figure 1F). We conclude that our organoid model consists of cell types involved in human anterior neurulation. Cells from embryos showed higher expression of hemoglobin subunits and other hypoxia-related genes, which may indicate hypoxic stress from sample handling or reflect differences in the metabolic environment ex vivo (Figure 1—figure supplement 1G; Schelshorn et al., 2009).

Identifying transcription factor candidates for regulation of anterior neurulation

Using our organoid model, we aimed to identify transcription factors driving anterior neurulation through a knockdown screen. Classical studies that physically disrupt the ectoderm during the neurula stages in vertebrates suggest that the neural ectoderm drives folding and closure of the neural plate (through elongation, tractoring, and/or bending), while the surface ectoderm is relatively passive (Jacobson, 1991; Karfunkel, 1974; Nikolopoulou et al., 2017). Therefore, we sought to identify transcription factors expressed within the neural ectoderm that drive this morphogenetic process. We ordered ectoderm cells along a pseudo-mediolateral coordinate using a diffusion map on scRNA-seq data from Day 2 (Figure 2A, left). We identified transcription factors expressed above a mean expression threshold across all cells and ranked them by the correlation of their expression with the mediolateral coordinate. This analysis revealed 20 transcription factors with highly specific expression in the neural plate (Figure 2A, right; Figure 2—figure supplement 1A, G, H). Thus, we selected these 20 transcription factors as candidates for a targeted knockdown screen.

Of these 20 factors, *ZIC2* has previously been shown to be required for anterior neural tube closure in the mouse embryo (Elms et al., 2003; Nagai et al., 2000). Before proceeding with a comprehensive knockdown screen of all 20 factors, we tested the role of *ZIC2* in regulating anterior neural tube closure in our organoid model. To knock down *ZIC2* using CRISPRi, we constructed a dual-guide RNA lentiviral transfer plasmid consisting of the top two *ZIC2*-targeting guide RNA sequences based on a published CRISPRi database (Replogle et al., 2022) and a control plasmid consisting of two non-targeting scramble guide RNA sequences. The guide RNA sequences on each plasmid were preceded by a mouse and human U6 promoter, respectively, and followed by a distinct direct capture sequence for scRNA-seq (Replogle et al., 2020). Each plasmid also carried a constitutive promoter driving mCerulean (Figure 2—figure supplement 1B). This dual-guide RNA construct is hereafter referred to as a ‘guide’ for brevity. In parallel, we generated a CRISPRi hPSC line in the H1/WA01 background expressing dCas9-KRAB under a constitutive promoter and confirmed that the CRISPRi construct was functional in the pluripotent state using *OCT4*-targeting guides (Figure 2—figure supplement 1C). We transduced CRISPRi hPSCs with lentivirus carrying either a *ZIC2*-targeting guide or a control non-targeting scramble guide. We differentiated lentivirus-transduced CRISPRi hPSCs into organoids as before, with 2 days of TGF β /WNT/BMP inhibition followed by 4 days of BMP4 exposure. All organoids transduced with a *ZIC2*-targeting guide ($N = 1$ biological replicate; $n = 6$ organoids) failed to undergo neural tube closure and displayed a persistent U-shaped neural plate, while all organoids transduced with a control scramble guide ($N = 1$ biological replicate; $n = 6$ organoids) formed closed neural tubes (Figure 2B). Thus, our organoid model recapitulated neural tube defects observed in *Zic2*-null mice, suggesting that *ZIC2* may similarly regulate anterior neurulation in humans.

To identify the genes regulated by *ZIC2* during neurulation, we performed scRNA-seq of Day 4 dCas9-KRAB organoids transduced with either the *ZIC2*-targeting guide or the control scramble guide. As before, we clustered cells into neural ectoderm, neural plate border, and surface ectoderm using SMD-derived marker genes from scramble control organoids (Figure 2—figure supplement 1D). In neural ectoderm cells, *ZIC2* knockdown reduced *ZIC2* expression by 60%, confirming the

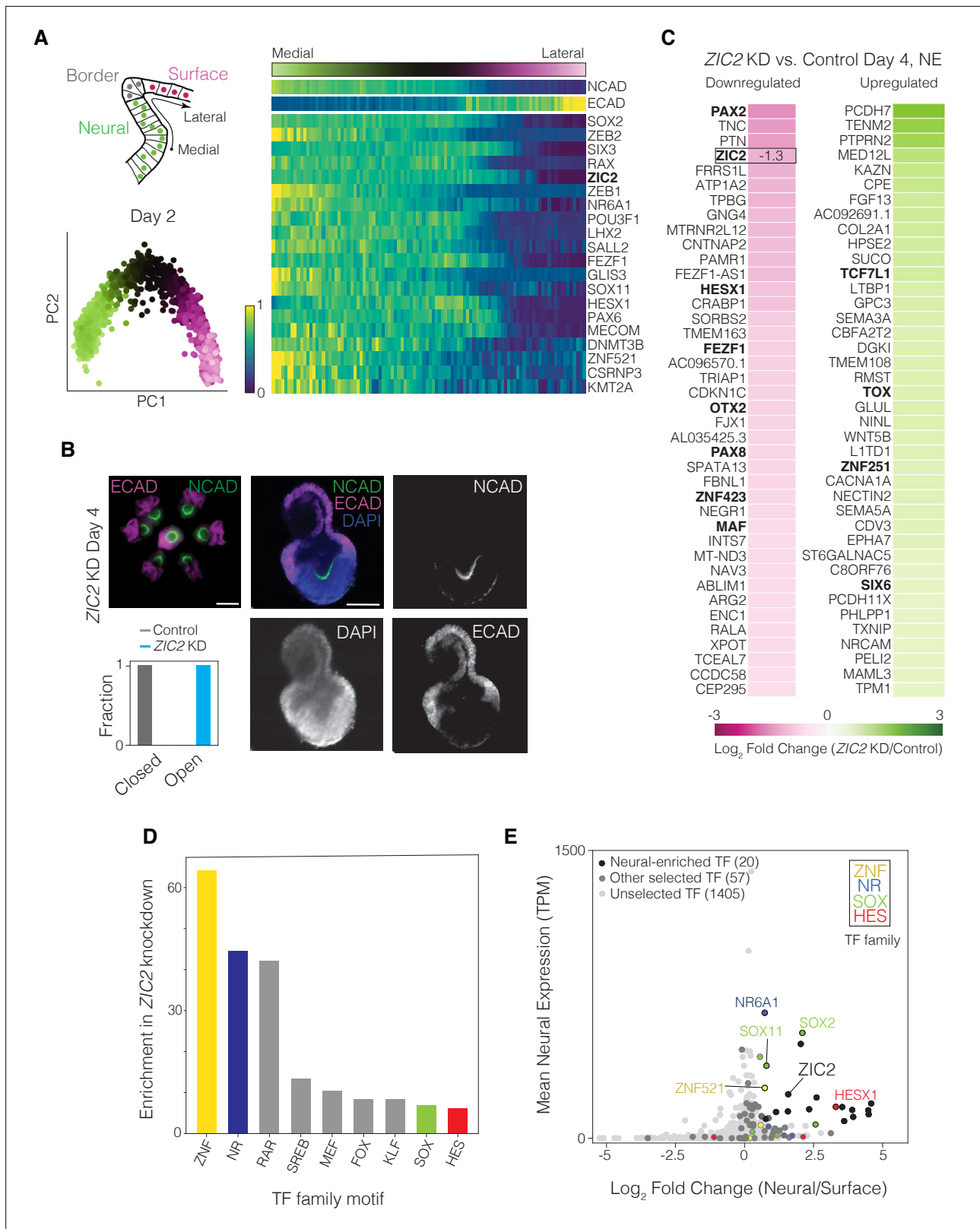


Figure 2. Identifying transcription factor candidates regulating anterior neurulation. **(A)** Top left: Illustration denoting the mediolateral axis present in neural tube organoids, spanning the dorsal neural ectoderm, neural plate border, and surface ectoderm. Bottom left: Principal component analysis of single-cell RNA-sequencing (scRNA-seq) data from Day 2 organoids, colored by pseudo-spatial mediolateral coordinate. Right: Standardized mediolateral expression profiles of NCAD, ECAD, and 20 most medially expressed transcription factors from Day 2 organoids. Mediolateral coordinate

Figure 2 continued on next page

Figure 2 continued

is denoted by the green-magenta color bar (top) and expression is denoted by the blue-yellow color bar (bottom left). **(B)** Day 4 organoids transduced with a dual-guide RNA targeting *ZIC2*. Top left: Epifluorescence merged-channel image of organoids on the pattern stained for NCAD and ECAD. Scale bar: 300 μm . Right: Confocal image of one organoid stained for NCAD, ECAD, and DAPI. Scale bar: 100 μm . Bottom left: Quantification of neural tube closure in Day 4 control and *ZIC2* knockdown (KD) organoids, showing that 0% of the control and 100% of *ZIC2* knockdown organoids possess an open neural plate. **(C)** Top 40 up- and downregulated genes in the neural ectoderm (NE) of Day 4 organoids upon *ZIC2* knockdown as compared to scramble control, based on \log_2 -normalized mean fold change (color bar, bottom). Transcription factors highlighted in bold. **(D)** Histogram of enrichment scores based on MEME SEA (Methods) of most overrepresented transcription factor family motifs in regulatory regions 10 kb upstream and 100 bp downstream of transcriptional start sites for the most downregulated genes upon *ZIC2* knockdown, using a threshold of \log_2 -normalized mean fold change relative to scramble control <-0.4 . Families are color-coded if a transcription factor from that family is present in our candidate selection (E). **(E)** Plot of mean expression in neural ectoderm (transcripts per million, TPM) versus \log_2 -normalized mean fold change in their expression between the neural and surface ectoderm in Day 2 organoids for all transcription factors ($n = 1482$). Top 20 most medially expressed transcription factors (black or black outline) and additional candidates (gray, $n = 58$) selected for knockdown ($n = 78$, total). Data points corresponding to members of TF family with enrichment of binding sites near *ZIC2*-regulated genes (D, Methods) are colored by family membership. All 78 candidates are listed in **Figure 2—figure supplement 1F**.

The online version of this article includes the following figure supplement(s) for figure 2:

Figure supplement 1. Transcriptome-based identification of candidate transcriptional regulators of anterior neurulation.

efficacy of the guide (**Figure 2C**). The proportion of neural ectoderm cells declined, and the neural plate border population expanded, suggesting that *ZIC2* loss altered cell fate proportions (**Figure 2—figure supplement 1E**). Notably, within the neural ectoderm, *ZIC2* knockdown led to differential downregulation of transcription factors including *PAX2*, *HESX1*, *FEZF1*, *OTX2*, *PAX8*, *ZNF423*, and *MAF* and upregulation of transcription factors *TCF7L1*, *TOX*, *ZNF251*, and *SIX6*, highlighting a potential gene regulatory network in the anterior neural plate (**Figure 2C**). We next examined regulatory regions upstream of genes strongly downregulated in Day 4 neural ectoderm cells upon *ZIC2* knockdown. Motif analysis revealed enrichment for binding sites associated with several transcription factor families, including ZNF, NR, SOX, and HES (**Figure 2D**, Methods). Five transcription factors from these families (*ZNF521*, *NR6A1*, *SOX2*, *SOX11*, and *HESX1*) appeared among the 20 transcription factors chosen for our knockdown screen based on their specific expression in the neural plate (**Figure 2A, E**, **Figure 2—figure supplement 1H**), further implicating them as candidates alongside *ZIC2* in co-regulating anterior neural tube closure.

We next sought to knock down our 20 candidate transcription factors in a high-throughput screen to test their roles in regulating neurulation using our organoid model. To serve as a contrasting control set for our selection criterion, we randomly selected an additional 58 transcription factors with medium to low neural specificity and a range of mean expression levels, giving us a total of 78 transcription factor candidates for our knockdown screen (**Figure 2E**, **Figure 2—figure supplement 1F**).

High-titer lentivirus production in small volumes enables high-throughput arrayed genetic screens in micropatterned hPSCs

Previous genetic screens in organoids have used pooled perturbations targeting multiple genes per organoid, creating mosaic tissues in which different cells carry distinct genetic modifications (**Fleck et al., 2023**). Although subsequent transcriptomic analyses in such studies revealed gene-specific effects on the transcriptional states of individual cells (**Figure 3A**, top), this mosaic approach is ill-suited for studying morphogenesis, which is driven by coordinated changes in cellular behavior across a tissue. First, localized genetic perturbations cannot be reproducibly targeted to areas of morphological interest; second, even if the perturbation happens to localize to the region of interest, it typically is present in too few cells to influence overall tissue shape. To overcome these limitations, we developed a method to knock down single genes individually throughout entire organoids in an arrayed format, allowing us to test their roles in tissue morphogenesis (**Figure 3A**, bottom).

To perform high-throughput arrayed knockdowns, we employed CRISPRi using a lentiviral library of dual-guide RNA constructs as above (**Replogle et al., 2020**). To select guides against each target, we selected the top two targeting guides based on a published CRISPRi database (**Figure 3—source data 1; Replogle et al., 2022**). To enable an arrayed screen, we modified the cloning workflow to perform insert annealing, ligation, and transformation in parallel. Before ligation, we applied stringent gel purification following dephosphorylation of the double-digested backbone to minimize backbone

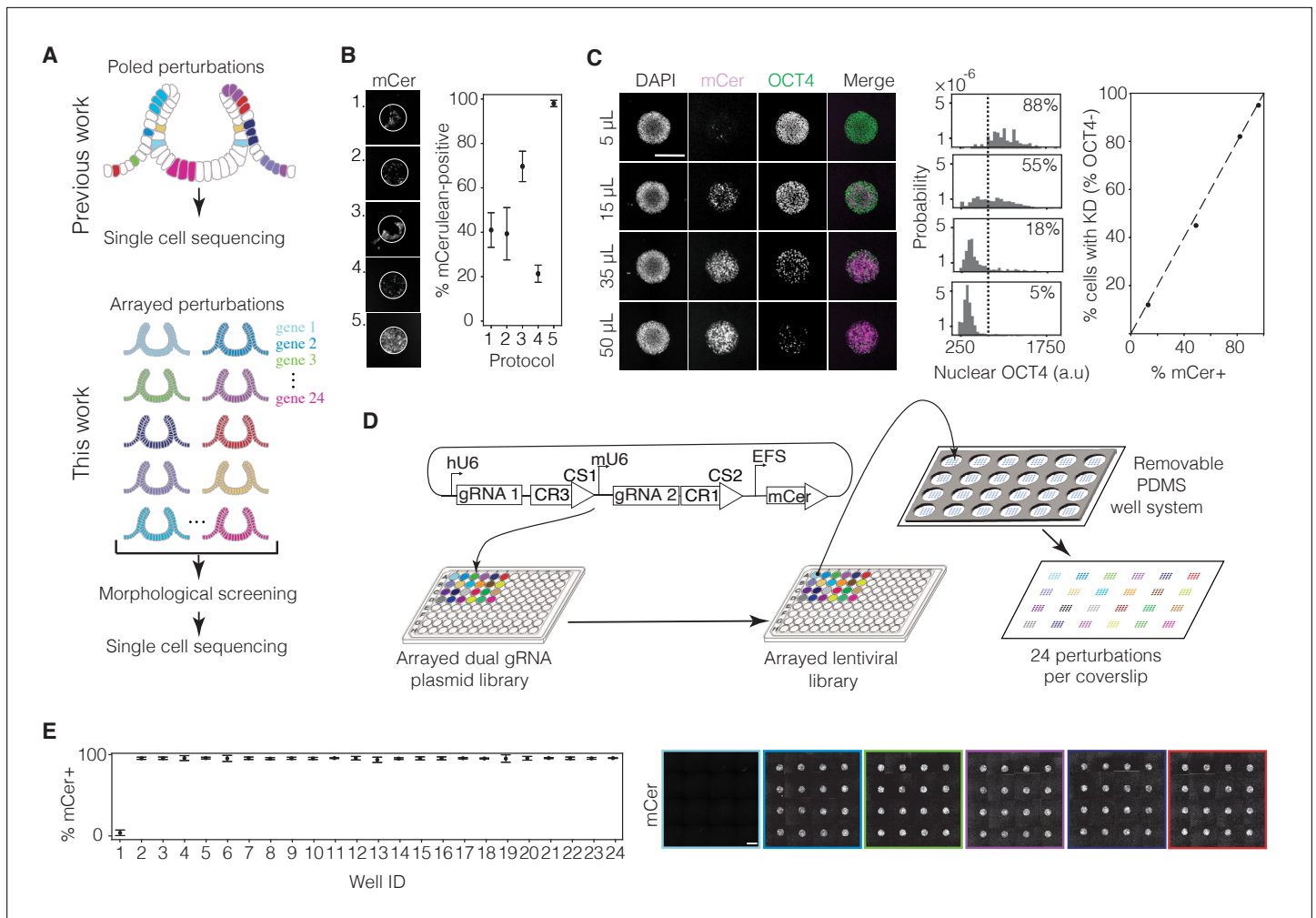


Figure 3. High-throughput method for arrayed single-gene perturbations. **(A)** Top: Schematic of pooled perturbations (as generated in previous work) that result in a mosaic organoid, in which a distinct sub-population of cells are perturbed by each guide RNA (shown in different colors). These mosaic organoids can be dissociated for single-cell transcriptomics. Bottom: Schematic of arrayed perturbations (generated in this work) that result in homogeneously perturbed organoids: all cells in each set of organoids are perturbed by the same guide (distinct guides shown in different colors). These organoids can be screened for morphological defects and subsequently dissociated and pooled for single cell transcriptomics. **(B)** Efficiency measurements of transduction protocols. Representative images (left) and quantifications (right) correspond to the following protocols. Protocol 1: Virus added 24 hr after seeding and incubated for 24 hr. Protocol 2: Virus added 24 hr after seeding and incubated for 1 hr. Protocol 3: Virus added 1 hr after seeding and incubated for 24 hr. Protocol 4: Virus added 1 hr after seeding and incubated for 1 hr. Protocol 5: Virus added during seeding and incubated for 1 hr. See **Figure 3—figure supplement 1D** for transduction efficiency calculation. **(C)** Correlation measurement of transduction and knockdown efficiencies. Left: Representative images of circular micropatterns show increasing transduction efficiency (mCerulean, mCer) and decreasing OCT4 expression with increasing viral volume of virus (volumes displayed left of each row) carrying a transfer plasmid with dual guides targeting OCT4, added to 150,000 human pluripotent stem cells (hPSCs) during seeding. Scale bar: 300 μm. Middle: Quantification of nuclear OCT4 fluorescence of individual cells in each condition. Dotted line (threshold) indicates 95th percentile value of OCT4 fluorescence in mCer- cells. Right top inset in each plot is the percentage of mCer+ cells with OCT4 fluorescence above the threshold, indicating OCT4 retention. Right: Plot of percentage of cells showing OCT4 knockdown versus percentage of cells that express mCer expressed by the guide plasmid show a positive correlation ($R^2 = 0.99$) demonstrating that live mCer fluorescence coverage of a micropattern is an accurate indicator of percentage of cells transduced. **(D)** Schematic of small-volume viral growth and 24-well organoid chip seeding. Dual gRNA plasmids are first arrayed in a 96-well plate. Different colors represent unique lentiviral transfer plasmids targeting different genes (**Figure 2—figure supplement 1B**). HEK cells are transfected in a 96-well plate to form an arrayed viral library, then applied to a glass coverslip containing micropatterned hPSCs (depicted with blue dots) using a temporary well system (depicted in dark gray). The well system is then removed, resulting in a glass chip with 24 sets of differently perturbed organoids, each with multiple replicates, that can be cultured in a single media condition. **(E)** Left: Quantifications of mCer fluorescence coverage of micropatterns in a mock-transduced well without virus (Well 1, 5% median mCer fluorescence coverage, $n = 16$ technical replicate micropatterns per well) and 23 scramble vector-transduced wells (Wells 2–24, 99% median mCer fluorescence coverage across wells, $n = 16$ technical replicate micropatterns per well). See **Figure 3—figure supplement 1D** for *Figure 3 continued on next page*

Figure 3 continued

calculation. Right: Stitched images of viral transduction of micropatterns in Wells 1–6. Transduction efficiency across wells is high and consistent, with a low cross-contamination rate. Scale bar: 300 μm .

The online version of this article includes the following source data and figure supplement(s) for figure 3:

Source data 1. Table with gRNA sequences chosen for each target gene.

Figure supplement 1. Development of transfection and transduction methods.

Figure supplement 1—source data 1. Original TIF files of gels in **Figure 3—figure supplement 1A**.

Figure supplement 1—source data 2. Labeled PNG files of gels in **Figure 3—figure supplement 1A**.

contamination, which yielded a high fraction of correctly ligated plasmids (**Figure 3—figure supplement 1A**). As a result, we were able to directly perform minipreps from bulk-transformed bacteria cultures without colony picking, thus streamlining the cloning process. Using this protocol, we successfully generated a plasmid library of dual-guide RNA constructs targeting 77 (including *ZIC2*) out of 78 transcription factor candidates, plus a scramble control.

Achieving high-efficiency lentiviral transduction of cells requires high concentrations of lentivirus. Existing protocols to generate lentivirus, which rely on ultra-centrifugation, PEG-based concentrator, or syringe filtration (*al Yacoub et al., 2007; Lee and Lee, 2018; Yuan et al., 2018*) are laborious and not amenable to high-throughput workflows. We thus developed an approach to enable efficient, single-gene knockdowns in organoids at high throughput. We first optimized 96-well plate virus production in HEK 293T cells by testing various transfection protocols, and we found that reducing media volumes during transfection and during viral production from HEK cells significantly increased viral titers (**Figure 3—figure supplement 1B, C**). We then compared hPSC transduction protocols on micropatterns. Standard protocols (Sigma-Aldrich) recommend adding virus 24 hr after seeding and incubating the cells with virus overnight. Using the percentage of the micropattern showing mCerulean fluorescence 48 hr post-transduction (**Figure 3—figure supplement 1D**) as a readout, we determined that virus treatment during cell seeding was far more efficient than virus treatment after seeding. We also found that 1 hr of virus treatment was sufficient to achieve high transduction efficiency. In contrast, 24 hr of high-titer virus treatment led to cell death (**Figure 3B**).

We hypothesized that enhanced transduction during cell seeding reflected increased exposure of the virus to the basolateral cell membrane of hPSCs. To test this, we transduced 3-day-old hPSC colonies with lentivirus after the formation of tight junctions and found that only colony edges were transduced. In contrast, transducing dissociated hPSCs during seeding led to uniform transduction (**Figure 3—figure supplement 1E**). These results are consistent with previous studies showing that the lentiviral VSV-G envelope protein interacts with the mammalian LDL receptor (LDLR), which is localized to the basolateral membrane of various epithelial tissues (*Finkelshtein et al., 2013*). This highlights the importance of performing viral transfection before the formation of tight junctions.

Our optimized protocol consistently achieved near-complete mCerulean expression of hPSCs on micropatterns. To determine whether mCerulean fluorescence coverage across a colony translated into efficiency of guide delivery at the level of individual cells, we cloned a transfer plasmid carrying a guide targeting the pluripotency factor OCT4 to measure knockdown in undifferentiated hPSCs. We found that 50 μl of virus grown in a 96-well plate of HEK 293T cells, when mixed with 50 μl of 150,000 CRISPRi hPSCs, was sufficient to deplete OCT4 in 95% of cells 48 hr post-transduction (**Figure 3C**). The percentage of cells showing OCT4 knockdown was highly correlated with mCerulean fluorescence coverage of the micropatterns (**Figure 3C**), confirming that mCerulean serves as a reliable live-cell reporter of transduction efficiency.

To perform arrayed knockdown of multiple genes in a single experiment, we needed to deliver distinct lentiviral plasmids, each carrying a different guide, to separate sets of micropatterned cells on the same coverslip. We therefore designed a PDMS stamp with 24 sets of circular micropattern features. Each set separated by the same center-to-center spacing of 9 mm matching the format of standard 96-well plates or multichannel pipettes. We also created a removable PDMS well system that could partition the coverslip into 24 fluid-separated wells or be removed to create a single well (**Figure 3D**). In parallel, we produced lentiviruses in small volumes in 96-well plates, with virus in each well carrying a unique guide (**Figure 3D**). To seed hPSCs, we coated the entire PDMS stamp with Matrigel and transferred it onto a 50-by-75 mm glass coverslip. Following Matrigel transfer, we

removed the stamp and replaced it with the PDMS well system. Using a multichannel pipette, we added a suspension of single hPSCs and lentivirus into each well (**Figure 3D**, Methods). After 70 min of incubation, we thoroughly rinsed and removed unadhered cells and unfused virus. 48 hr later, we assessed mCerulean fluorescence coverage of micropatterns. Our protocol resulted in highly reproducible transduction of micropatterned hPSC colonies in an arrayed format, with a median transduction efficiency of 99% (**Figure 3E**). The PDMS well system prevented viral cross-contamination between neighboring wells, as seen by the less than 5% transduction of the untreated control well. Transduced hPSC colonies could then be differentiated into anterior neural tube organoids to model the effects of single-gene perturbations on neural tube morphogenesis.

A high-throughput genetic screen of anterior neurulation reveals three transcription factors necessary for proper neural tube closure

We cloned guide plasmids (Methods) against 77 out of our 78 transcription factor candidates (**Figure 2E**, **Figure 2—figure supplement 1F**). Using our screening method, we conducted a high-throughput arrayed CRISPRi knockdown screen of these 77 factors to evaluate their individual roles in anterior neurulation (**Figure 2—figure supplement 1E**). We included *ZIC2* and a scramble control in this screen for methodological consistency with all other factors. Guide plasmids in our screen yielded a mean transduction efficiency of 93% (**Figure 4—figure supplement 1A, B**), slightly lower than the 99% we achieved with a clonal guide (**Figure 3E**), perhaps due to mis-ligated products in the non-clonal plasmid population (Methods). After seeding and transducing hPSCs, we differentiated them into organoids using our protocol (**Figure 1—figure supplement 1D**). Organoids were fixed after 4 days of BMP4 exposure, stained for NCAD and ECAD, and screened for morphological defects using epifluorescence microscopy. Analysis of guide expression at the end of the differentiation time course, as measured by mCerulean, showed retention of lentiviral gene expression throughout the experiment (**Figure 4—figure supplement 1F**).

We focused particularly on neural tube closure defects, as assessed by a lack of continuous NCAD staining enclosing the neural lumen. Lumen morphology was clear from epifluorescence microscopy for all candidates except *RFX7* and *ZNF521*, which required confocal microscopy for phenotypic categorization (**Figure 4B**, **Figure 4—figure supplement 1C**). Most candidates had no closure defects (score = 0, **Figure 4A–C**, **Figure 4—figure supplement 1D**). Knockdown of 24 transcription factors (*HESX1*, *TGIF1*, *ZFH4*, *MAFB*, *TSHXZ2*, *ZNF219*, *PAX3*, *ID3*, *PBX3*, *SP5*, *POU3F2*, *SSRP1*, *TLX2*, *VSX2*, *DNMT1*, *CSNRP3*, *TFDP2*, *DNMT3B*, *ZNF280*, *MSX1*, *SALL3*, *PLAGL1*, *SALL4*, and *ARX*) showed minor closure defects upon knockdown, where a fraction of organoids showed either a small opening in the neural plate or delayed neural tube closure compared to control organoids (score = 1, **Figure 4A–C**, **Figure 4—figure supplement 1E**). For example, organoids with a *HESX1* knockdown showed a minor opening in the neural plate on Day 4 (**Figure 4C**), which resolved after an additional day of differentiation in five out of six organoids (**Figure 4B**).

Knockdown of three transcription factors (*ZIC2*, *SOX11*, and *ZNF521*) showed major closure defects upon knockdown (score = 2) consistently across all organoids in three biological replicates consisting of 6 organoids each (**Figure 4A–C**). Confocal microscopy of *ZIC2* and *SOX11* knockdown organoids showed that their neural plates were fully open, while confocal microscopy of *ZNF521* knockdown organoids showed multiple discontinuous regions of surface ectoderm on top of the neural ectoderm, which we interpreted as multiple points of closure (**Figure 4C**).

To quantify the knockdown efficacy of CRISPRi guides in organoids, we performed scRNA-seq on Day 4 organoids with arrayed knockdowns of the transcription factors that showed a major phenotype (*ZIC2*, *SOX11*, and *ZNF521*). To determine false negative rates or minor phenotypes as a result of poor knockdown efficacy, we also sequenced organoids corresponding to knockdowns of six transcription factors that did not show a closure defect (*OTX2*, *PAX6*, *POU3F1*, *LHX2*, *TOX3*, and *GLI3*) and two transcription factors that showed a minor defect (*TGIF1* and *ZFH4*). Because each guide included a constant region tagged with a direct capture sequence readable by scRNA-seq (**Replogle et al., 2020**), we could pool the arrayed samples prior to single-cell library preparation to reduce costs (**Figure 2—figure supplement 1B**). Guide targets *ZIC2*, *SOX11*, and *ZNF521* were among the most downregulated transcripts within the neural ectoderm in each knockdown condition, respectively (boxed data, **Figure 5A**, **Figure 5—figure supplement 1A, B**), showing that targeted knockdown was successful. Knockdown efficacies of guides that did not show a phenotype or showed only a minor

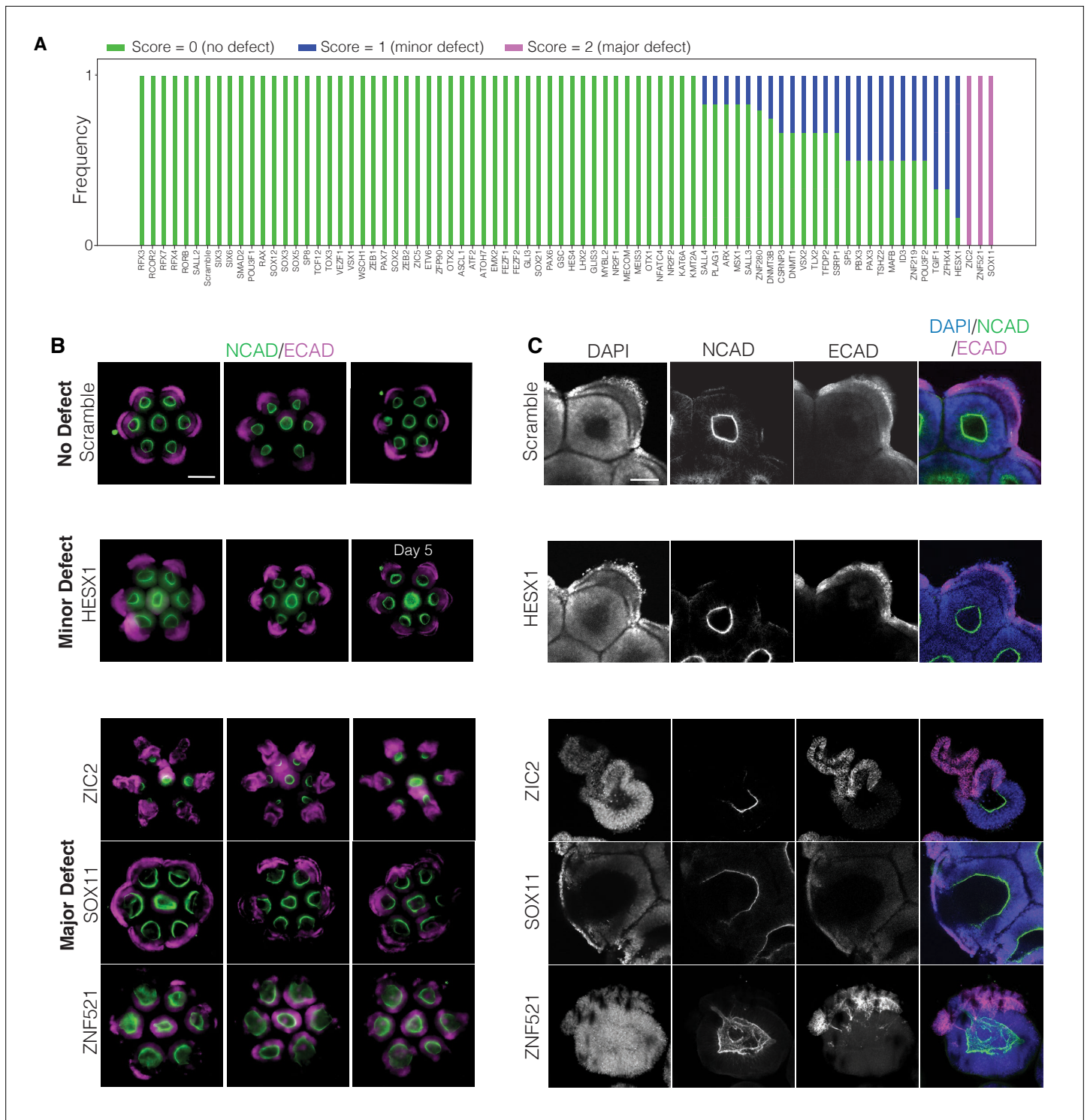


Figure 4. *SOX11*, *ZIC2*, and *ZNF521* are necessary for neural tube closure. **(A)** Phenotypic scores of organoids knocked down with each gene. Scoring was based on whether organoids had no closure defects (score = 0, white), a minor defect (score = 1, gray), or a major defect (score = 2, black) consisting of either a fully opened neural plate or multiple closure points. **(B)** Epifluorescence microscopy of organoids at Day 4 (unless otherwise noted), showing examples of no defect (top row, scrambled control), minor defect scores (*HESX1* knockdown, row 2), or major defect scores (*ZIC2*, *SOX11*, and *ZNF521* knockdown, rows 3–5, respectively). Three biological replicates per condition are shown with $n = 6$ outer organoids per biological replicate. Imaging of *HESX1* knockdown organoids with a minor defect on Day 5 shows that most of them eventually close and that minor openings represent delayed closure. Scale bar: 300 μm . **(C)** Corresponding confocal images of single organoids for each of the phenotype classes in **(B)**, showing a range of closure phenotypes. Scale bar: 100 μm .

Figure 4 continued on next page

Figure 4 continued

The online version of this article includes the following figure supplement(s) for figure 4:

Figure supplement 1. Perturbation of most transcription factors does not give rise to morphological phenotypes.

phenotype were comparable to knockdown efficacies of *ZIC2* and *ZNF521*, with seven out of eight chosen guides showing significant knockdown (**Figure 5—figure supplement 1C**).

Consistent with our hypothesis that the neural plate drives neurulation, the three transcription factors whose knockdown most significantly disrupted neural tube closure (*ZIC2*, *SOX11*, and *ZNF521*) were all among the list of 20 transcription factors chosen based on specific expression in the neural ectoderm (**Figure 2A**). Notably, strong phenotype-producing factors *SOX11* and *ZNF521* and minor phenotype-producing factor *HESX1* all belonged to transcription factor families with associated motifs at regulatory regions near *ZIC2* target genes (**Figure 2D, E**). This suggests the possibility of a coordinated transcriptional program within the neural ectoderm downstream of these factors.

Deciphering the gene networks regulating anterior neurulation

Morphologically, *ZIC2* and *SOX11* knockdowns resulted in a persistently open neural plate, whereas *ZNF521* knockdown gave rise to multiple discrete closure points, suggesting opposing roles (**Figure 4B, C**). Phenotypically, these results suggest that *ZIC2* and *SOX11* promote neural tube closure, while *ZNF521* has an opposing role. To determine whether the phenotypic similarities and differences of *ZIC2*, *SOX11*, and *ZNF521* knockdowns are reflected in the gene regulatory functions of these factors, we analyzed single-cell gene expression data from perturbed organoids.

We analyzed scRNA-seq data from Day 4 organoids in which each of these three transcription factors were knocked down to evaluate changes in gene expression relative to control organoids. Hierarchical clustering of genes expressed in neural ectoderm from control organoids revealed nine modules of co-regulated genes (**Figure 5B**). One module, consisting of *ZIC2* and several other neural transcription factors and markers, was significantly downregulated following *SOX11* knockdown (**Figure 5C, Figure 5—figure supplement 1D**), consistent with the enrichment of *SOX* family binding motifs at regulatory regions near *ZIC2*-regulated genes (**Figure 2D**).

We next examined genes that were significantly downregulated in the neural ectoderm in at least two of three knockdowns of *ZIC2*, *SOX11*, and *ZNF521*, compared to the scramble control (Anderson–Darling test, $p < 0.05$, **Figure 5D**). Of these genes, those affected by both *SOX11* and *ZIC2* knockdown showed larger fold decreases than all other pairs of knockdowns, as reflected by the relative number of genes in the lower left quadrants of fold change plots comparing knockdown pairs (**Figure 5D**, scatterplots). Many of these genes also ranked highly in their degree of downregulation when compared to all other genes upon *SOX11* or *ZIC2* knockdown (**Figure 5A**). These observations suggested that *SOX11* and *ZIC2* jointly drive a gene regulatory program consisting of a shared set of genes, including *PAX2*, *PTN*, *GNG4*, *HESX1*, *FRRS1L*, *CRABP1*, *SORBS2*, *TMEM163*, *PAX8*, and *NEGR1* (from bottom left to top right in **Figure 5D**). Of these genes, *PAX2* knockouts show fully penetrant exencephaly, although at the midbrain level rather than forebrain (Püschel et al., 1992; Torres et al., 1996), and *CRABP1* single-nucleotide polymorphisms have been found in human patients with spina bifida and exencephaly (Li et al., 2018).

Consistent with the opposing role of *ZNF521* suggested by its knockdown phenotype, several genes that were significantly ($p < 0.05$) downregulated upon *ZIC2* or *SOX11* knockdowns were upregulated upon *ZNF521* knockdown (**Figure 5E**). Four of these genes, including neural tube literature candidates *PAX2* and *CRABP1*, were significantly downregulated upon both *ZIC2* and *SOX11* knockdown and significantly upregulated upon *ZNF521* knockdown (*PAX2*, *CRABP1*, *TMEM163*, and *ARL4C*; **Figure 5E**).

We next asked whether we could phenocopy a neural tube closure defect by knocking down genes downstream of *ZIC2*, *SOX11*, and *ZNF521*. We selected 10 genes that were most co-downregulated by *SOX11* and *ZIC2*, including *PAX2*, *PTN*, *GNG4*, *HESX1*, *FRRS1L*, *CRABP1*, *SORBS2*, *TMEM163*, *PAX8*, and *NEGR1* (**Figure 5D**). We also chose *ARL4C*, which was significantly downregulated upon *SOX11* and *ZIC2* knockdown and significantly upregulated upon *ZNF521* knockdown, along with *CRABP1*, *PAX2*, and *TMEM163* (**Figure 5E**). Apart from *HESX1*, which showed a minor closure defect (**Figure 4A–C**), there was no single gene in this set whose knockdown alone recapitulated the open neural plate phenotype observed upon *ZIC2* or *SOX11* knockdown (**Figure 5—figure supplement**

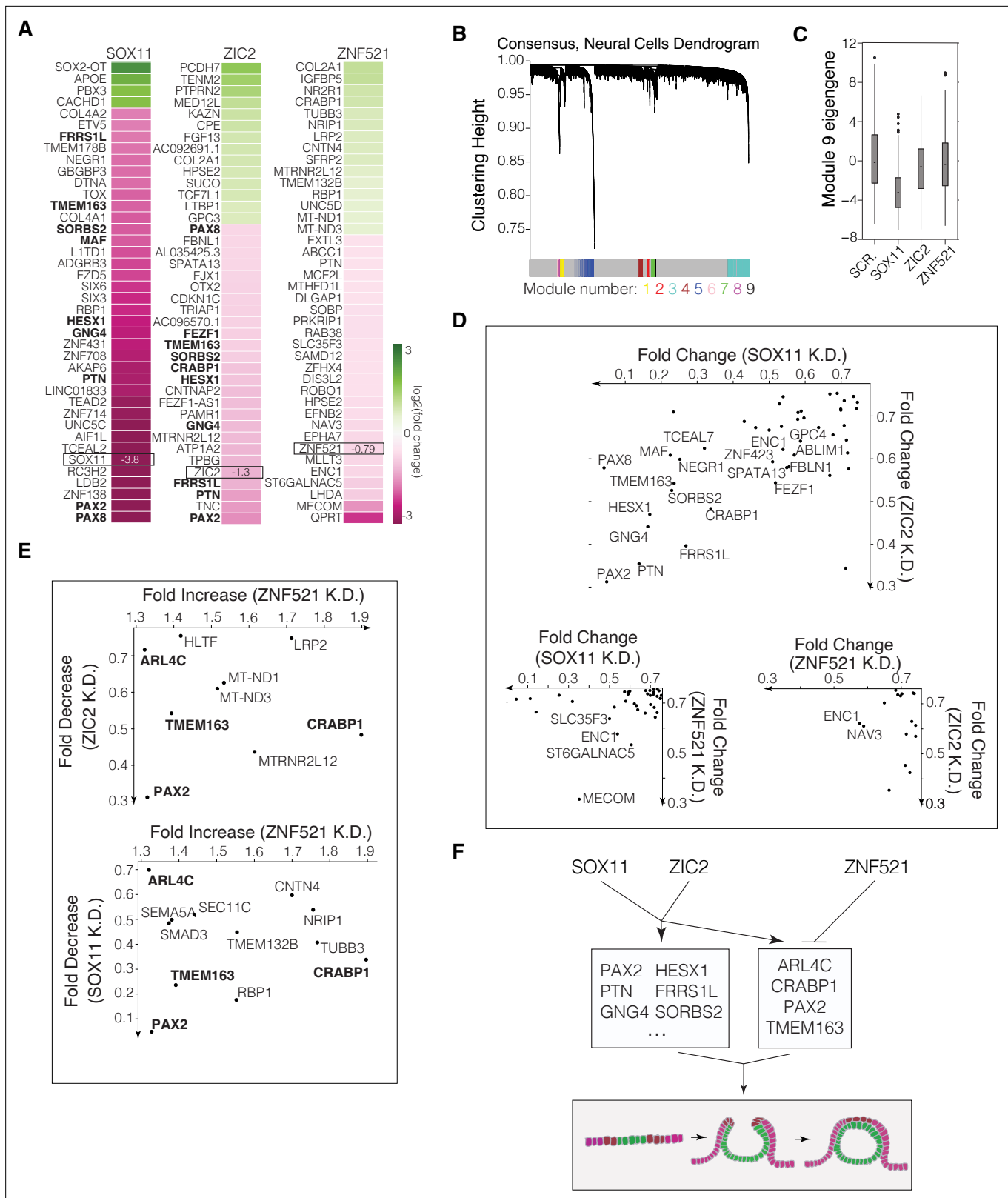


Figure 5. *SOX11* and *ZIC2* co-regulate a shared set of genes in opposition to *ZNF521*. **(A)** Log₂-normalized mean fold changes of the 40 most up- or downregulated genes in the neural ectoderm of each knockdown condition at Day 4, as compared to organoids transduced with a scramble control guide. Genes that are co-downregulated by *SOX11* and *ZIC2* knockdown are shown in bold. **(B)** Cluster dendrogram of WGCNA analysis of single-cell RNA-sequencing (scRNA-seq) gene expression from neural cells (scramble control) showing modules of co-expressed genes. Module assignment

Figure 5 continued on next page

Figure 5 continued

(numbered) is indicated by the color bar; genes labeled in gray were not assigned. (C) Module eigengene values (representative first principal component of expression of genes in a module) of Module 9 per cell in the neural cell population in each knockdown condition compared to scramble control data. *SOX11* knockdown leads to significant downregulation of genes in Module 9 ($p < 0.0001$) by t-test (chosen to see if there was a significant difference between mean eigengene values between control and perturbed datasets), which includes *ZIC2* (see **Figure 5—figure supplement 1D**). (D) Scatterplots showing \log_2 -normalized mean fold changes of significantly co-downregulated genes (Anderson–Darling test, $p < 0.05$) in the neural cell populations from transcription factor knockdown pairs, as compared to organoids transduced with a scramble control guide. Genes are plotted if their \log_2 -normalized mean fold change in expression relative to scrambled control is less than < -0.4 in both knockdown conditions. Genes are labeled if this value is less than < -0.6 in both conditions. (E) Scatterplots showing fold changes of genes that are significantly downregulated (Anderson–Darling test, $p < 0.05$) by *ZIC2* or *SOX11* knockdown and significantly upregulated by *ZNF521* knockdown, as compared to organoids transduced with a scramble control guide. (F) Gene regulatory model: *SOX11* and *ZIC2* are upstream a similar set of genes, including neural tube defect candidates from the literature like *PAX2*, *HESX1*, and *CRABP1*. *ZNF521* upregulates a separate set of genes but downregulates several shared *ZIC2*- and *SOX11*-upregulated genes.

The online version of this article includes the following figure supplement(s) for figure 5:

Figure supplement 1. Analysis of single-cell RNA-sequencing (scRNA-seq) data from perturbed organoids.

1F. These findings argue that *ZIC2*, *SOX11*, and *ZNF521* do not act through a single dominant downstream effector and instead regulate a combination of genes to drive anterior neurulation.

Discussion

Perturbing the expression of genes individually and uniformly in hPSC-derived tissues is essential to determine their roles in morphogenesis during human embryonic development. The arrayed CRISPRi platform developed in this study allowed us to screen transcription factors in an hPSC-derived organoid model of anterior neurulation, revealing that three key transcription factors, *ZIC2*, *SOX11*, and *ZNF521*, act together to drive neurulation in the forebrain region. Knocking down these transcription factors shows opposing phenotypes, with *ZIC2* and *SOX11* knockdown resulting in an open neural plate and *ZNF521* knockdown leading to multiple points of neural tube closure. Our analyses of gene expression changes upon *ZIC2* and *SOX11* knockdown suggest that these two transcription factors regulate a shared set of gene targets. Consistent with the opposite phenotype of *ZNF521*, we find that *ZNF521* downregulates several of the gene targets upregulated by both *ZIC2* and *SOX11*. The set of these oppositely regulated factors includes *PAX2* and *CRABP1*, which have been previously implicated in anterior neural tube defects in mice and humans, respectively (Püschel et al., 1992; Torres et al., 1996; Li et al., 2018).

Our results suggest that coordinated transcriptional regulation of downstream gene targets by *ZIC2*, *SOX11*, and *ZNF521* is necessary for successful anterior neurulation in vitro (Figure 5F). The role of *ZIC2* in neurulation has been well characterized in vivo in mouse (Elms et al., 2003; Nagai et al., 2000), and genetic variants of *SOX11* in humans have been associated with midline defects, microcephaly, and ocular malformations (Al-Jawahiri et al., 2022; Hempel et al., 2016). In mouse, *SOX11* deficiency leads to grossly normal neurulation in mice despite causing other broad morphological defects, suggesting possible species-specific differences in *SOX11*'s developmental roles (Sock et al., 2004). As human anencephaly is embryonic lethal, genetic causes have only been obtained in rare cases with whole exome sequencing (Bonnard et al., 2020; Singh et al., 2017). This raises the possibility that *ZIC2*, *SOX11*, and *ZNF521* also drive neurulation in vivo. In the future, it will be of interest to identify more genes with de novo mutations contributing to anencephaly in human embryos, as has recently been conducted for spina bifida (Ha et al., 2025).

The ability to perform single-gene perturbations in robust in vitro models of human development is essential for dissecting the mechanisms that drive human embryonic morphogenesis. Until now, this goal has been limited by variability in organoid morphogenesis and the lack of scalable methods for uniform single-gene perturbations. The platform we report here integrates a micropatterned hPSC-based protocol to generate reproducible organoids with uniform single-gene knockdown via lentivirus-mediated arrayed CRISPRi to identify genes with roles in morphogenesis. Furthermore, the method reduces costs compared to clonal knockdown approaches, is scalable, and can be performed in an academic laboratory setting, enabling tissue-wide single-gene perturbations at a scale that has not been previously feasible either in organoids in vitro or in mammalian models in vivo. Our approach

bridges a critical gap between the genetic study of traditional model organisms and human developmental biology, offering a path for new mechanistic insights and the discovery of therapeutic targets for neural tube defects and other congenital malformations.

Limitations of the study

The first limitation of this study is that inherent to any method that utilizes CRISPR: the efficacy of selected guides. Based on quantification of gene knockdown by scRNA-seq, we estimate that 87% of targeting guides were effective in our system. The second limitation is the assumption that the genes we discovered in vitro are relevant in humans in vivo. False positives or false negatives could arise in part due to the study of isolated tissues in vitro that lack surrounding cell types, which may either compensate for or trigger tissue-level defects. Given the increasing fidelity of organoid models in terms of their ability to recapitulate the complexity of fetal tissues, we believe that this limitation will be overcome in time. While in vitro systems are ultimately models, they serve as a complement to in vivo studies to increase our understanding of human development and disease, and they offer value in their amenability to high-throughput perturbations.

Methods

Cell lines

Human stem cell work was performed in accordance with Institutional Review Board (IRB) protocol IRB23-0937. Neural tube organoid differentiation was optimized in an H1 OTX-YFP hESC line (gift from the Allen Institute). Knockdown experiments were conducted with an H1 DCX-YFP hESC line (gift from the Allen Institute) modified by inserting pAAVS1-NDi-CRISPRi into the AAVS1 locus. pAAVS1-NDi-CRISPRi (Gen1) was a gift from Bruce Conklin (Addgene plasmid #73497; <http://n2t.net/addgene:73497>; RRID:Addgene_73497). dCas9 integration was validated with genotyping, and CRISPRi activity was validated with OCT4 knockdown. The H1 background line has XY chromosomes and was chosen because of our extensive experience in the lab with this line. We recognize the value of studying lines with other genotypes in order to learn sex-specific mechanisms of human development. As there is considerable line-to-line variability in stem cell models (*Ortmann and Vallier, 2017*), this work provides one benchmark against which to compare XX other XY lines. All research in this study falls under International Society for Stem Cell Research Category 1a.

hESCs were grown in 6-well culture dishes (CellTreat) pre-treated with diluted Matrigel hESC-qualified Matrix (Corning Cat No. 354277) according to the manufacturer's instructions and fed with mTeSR Plus (StemCell).

hESCs were maintained via colony-passage every 4 days with ReLeSR (StemCell) according to the manufacturer's instructions. Colonies were broken into clumps of 5–15 cells and diluted 1:30 into a new maintenance plate using wide-bore pipette tips. Cells were fed with fresh mTeSR Plus every 2 days. Cell lines were routinely tested for mycoplasma contamination (Mycoplasma PCR Detection Kit, ABM G238).

hESCs were expanded for experiments via single cell passage to ensure consistent cell density. 10-cm culture dishes were pre-treated with Matrigel according to the manufacturer's instructions. Maintenance hESC wells were rinsed with PBS, treated with Accutase (Innovative Cell Technologies) for 5–10 min, spun down and aspirated, and rescued in mTeSR Plus with 10 μ M ROCK inhibitor (Y-27632, Stemgent). 500,000 cells were added to a 10-cm dish with 10 ml of mTeSR Plus with 10 μ M Y-27632. After 24 hr, cells were switched to mTeSR Plus without Y27632. Cells were fed with fresh mTeSR Plus every day for optimal growth and expanded for a total of 4 days before experimental seeding.

Lentivirus was grown in Lenti-X 293T HEK cells (Takara Bio). HEK cells were grown in deep 10-cm tissue culture dishes (Nunc) and fed with 10% fetal bovine serum (FBS, Millipore) in DMEM/F12 (Thermo). Cells were passaged at a dilution ratio of 1:10 every 3 days with 0.25% Trypsin-EDTA (Life Technologies) according to the manufacturer's instructions.

Bacterial transformations were performed in NEB Stable Competent *E. coli* (NEB C204OH) according to the manufacturer's instructions.

Soft lithography and microcontact printing

Photomasks were designed in AutoCAD and submitted to Artnet Pro (formerly CAD/Art) for printing. For the neural tube model, circles were arranged in hexagons with a diameter of 250 μm per circle and edge-to-edge circle spacing of 100 μm . For transduction efficiency optimization experiments, circles were arranged in 4 \times 4 format with a diameter of 350 μm per circle and inter-circle spacing of 1000 μm . For 24-well format, 24 sets of hexagons or 4 \times 4 grids were arranged with an inter-well spacing of 9 mm for compatibility with 96-well and multichannel pipette spacing.

Microcontact printing was performed as in [Anand et al., 2023](#). Briefly, 50- μm thick 73-mm diameter dry photoresist films (ADEX, DJ Microlaminates) were laminated onto silicon wafers (University Wafers) using a SKY 335R6 laminator (SKY-DSB Co., Ltd) at a temperature of 65°C. Photomasks were placed on top of the photoresist under a long pass filter (PL-360LP, Omega) and then cured under a 365-nm UV lamp (Uvitron) for 16 s at an intensity of 25 mW/cm². Silicone and photoresist were developed in cyclohexanone (Sigma) for 5 min before rinsing with acetone and then isopropanol, then drying with a stream of compressed air. Resulting molds were baked on a glass dish on a Cimarec hot plate (Thermo) at 150°C for 1 hr and then placed in a 10-cm Petri dish and silanized with 50 μl of Trichloro(1H,1H,2H,2H-perfluorooctyl)silane (Sigma) on a glass slide in a vacuum chamber overnight. PDMS (Ellsworth Adhesives) was mixed at a curing agent:base reagent ratio of 1:10 and vacuum-treated for 30–60 min to remove air bubbles. 20–40 g of PDMS were poured into a Petri dish containing the silicone mold, and the dish was baked in an oven (VWR, Sheldon Manufacturing) at 80°C for 2 hr. Stamps were cut out of the dish in a biosafety cabinet in the shape of their rectangular circumference and sterilized by UV treatment under a germicidal lamp for 20 min.

Matrigel hESC-qualified Matrix (354277, Corning) was diluted at double the concentration recommended by the manufacturer's instructions in DMEM/F12 media. 5 ml of diluted Matrigel was added to each stamp and left to polymerize overnight at room temperature before seeding.

24-Well design and construction

24-Well sticker templates were designed in Silhouette Studio with a well diameter of 8 mm and an inter-well distance of 9 mm for compatibility with 96-well and multichannel pipette spacing. Stickers were printed using a Silhouette Cameo cutting machine.

PDMS was mixed and vacuum-treated as above. 20 g of PDMS was poured into an empty Petri dish, and the dish was baked at 80°C for 2 hr. PDMS was cut out from the dish in a biosafety cabinet and placed in the Petri lid for cutting. The 24-well sticker template was applied, and wells were cut out in a biosafety cabinet using an 8-mm biopsy punch (Ted Pella). Well systems were UV-treated for 20 min on each side for disinfection.

Neural tube organoid differentiation

For neural tube organoid protocol optimization, cells were seeded on glass coverslips as in [Anand et al., 2023](#). Briefly, glass coverslips were cut to fit wells of a 6-well plate, sprayed with ethanol, and dried with compressed air in a biosafety cabinet. Matrigel-coated PDMS hexagon stamps were rinsed in distilled water, dried with compressed air, and applied to the center of the coverslip for several minutes in order for Matrigel transfer to occur. Gentle pressure was applied to the stamp to help with transfer. The stamp was then removed for seeding.

Expanded hESCs were rinsed with PBS and treated with Accutase for 15 min at room temperature. Cells were then collected, spun down for 3 min at 200 rcf, aspirated, resuspended at 3 million cells/ml in mTeSR Plus with 10 μM Y27632. The well was filled with cells suspended at 1–2 million cells/ml and incubated for 1 hr in a tissue culture hood to form attachment to the Matrigel. Wells were then rinsed with DPBS (Lonza), the well system was removed, and the plate received one final rinse in DPBS before the addition of fresh mTeSR Plus with 10 μM Y27632. 24 hr post-seed, media was changed to mTeSR Plus without Y27632.

Neural tube differentiation was initiated at 48 hr post-seed (Day –2) in N2B27 media. Small molecule and signaling protein concentrations were optimized as described in [Figure 1—figure supplement 1B, C](#). The optimized protocol was as follows: Ectodermal differentiation was initiated at Day –2 with N2B27+10 μM LDN +5 μM SB+1 μM IWP3+5% Matrigel by volume. On Days 0 and 2, media was replaced with N2B27 + 10 ng/ml BMP4 + 5 μM SB + 3 μM IWR1 + 5% Matrigel by volume. Total volume for a 6-well plate was 2 ml, while the total volume for a 10-cm plate was 12 ml.

Plasmid design and cloning

A dual guide lentiviral transfer plasmid backbone was designed according to *Replogle et al., 2022*, with the payload hU6-guide1-CR3^{CS1}-mU6-guide2-CR1^{CS2}-EF1alpha-mCerulean. Two guide sequences against each gene were selected according to *Replogle et al., 2022*. Transfer plasmids were cloned as in *Replogle et al., 2022*, but modified to utilize arrayed oligo annealing and ligation. Briefly, a backbone containing hU6-CR1^{CS2}-EF1alpha-mCerulean was double digested with BsmBI-v2 (NEB) between the hU6 and CR1 and treated with Quick CIP (NEB). Oligo strands with 4-basepair overhangs were annealed and ligated with backbone and a gBlock containing CR3^{CS1}-mU6 using T4 ligase (NEB) as previously described (*Figure 3—source data 1; Replogle et al., 2020*), but in arrayed 96-well format. NEB Stable (NEB) bacteria were transformed with each plasmid in 96-well plates using heat shock for 30 s at 42°C in a thermocycler. Bacteria were rescued in 1 ml SOC media (Thermo Fisher) and grown in 5 ml LB media (Thermo Fisher) with 100 µg/ml carbenicillin overnight at 30°C on a rotating roller drum before miniprep (QIAGEN). For clonal plasmid preparation, 50 µl from 5 ml overnight cultures were plated uniformly on LB + Carbenicillin plates (Teknova) using autoclaved glass beads, grown for 24–48 hr at 30°C, and re-inoculated into overnight liquid culture prior to miniprep. Double digest assay was performed with DraIII-HF (NEB) and BamHI-HF (NEB). Sanger sequencing of the insert was performed using a forward or reverse primer flanking the insert site via Genewiz from Azenta. Whole plasmid sequencing was performed via Plasmidsaurus. We were unable to clone a plasmid with guides against NR6A1 that showed any CFP expression, perhaps due to toxicity of the guides.

Lentiviral production in 96-well format

Lentiviral particles carrying each gRNA were grown in Lenti-X 293T HEK cells in 96-well tissue culture plates (Celltreat). HEK cells were first passaged via Trypsin according to the manufacturer's instructions and seeded at 60,000 cells/well. HEK cells were transfected when 60–95% confluent, about 24 hr post-seed. Transfection reagents were prepared in 96-well PCR plates (VWR). A master mix of 13 ng/µl pMDLg/pRRE, 9 ng/µl pRSV-Rev, and 4.3 ng/µl pMD2.G was deposited into each well at 3 µl/well. pMDLg/pRRE, pRSV-Rev, and pMD2.G were gifts from Didier Trono (Addgene plasmid # 12251; <http://n2t.net/addgene:12251>; RRID:Addgene_12251; Addgene plasmid # 12253; <http://n2t.net/addgene:12253>; RRID:Addgene_12253; Addgene plasmid # 12259; <http://n2t.net/addgene:12259>; RRID:Addgene_12259). Transfer plasmids at 17.6 ng/µl were deposited into each well at 3 µl/well. A master of jetPrime reagent diluted 1:16 in jetPrime buffer was deposited in each well at 3 µl/well, and all 9 µl of well content were thoroughly mixed and incubated for 10 min. After incubation, 91 µl of 10% FBS-DMEM/F12 was added to each reagent well. HEK plates were aspirated, and media was replaced with 100 µl 10% FBS-DMEM/F12 and transfection reagents. Four hours later, BSL2+safety media change was performed into 70 µl of fresh 5% FBS-DMEM/F12. Virus was allowed to grow for 48 hr before transduction.

Microcontact printing and hPSC seeding in 24-well format

24-Well systems were prepared as follows in a biosafety cabinet immediately before seeding: A 50 mm by 75 mm borosilicate glass coverslip (Brain Research Laboratories) was sprayed with ethanol, dried with compressed air, and placed in the lid of a deep 10-cm tissue culture dish (Nunc). Matrigel-coated stamps were aspirated, rinsed in MilliQ water, dried with compressed air, and applied to the center of the coverslip for several minutes in order for Matrigel transfer to occur. Gentle pressure was applied to the stamp to help with transfer. The 10-cm plate bottom was applied to hold the coverslip in place, and the plate was up to mark the corners of the stamp with a pen on the bottom of the plate. The plate was then returned to the biosafety cabinet, the plate bottom taken off, and the stamp removed carefully to keep the coverslip aligned with the markings. The 24-well PDMS was applied to the coverslip in alignment with the stamp markings and pressed forcefully to create a seal with the coverslip. A diamond-tip scribe (Techni-tool) was used to trim the lateral edges of the coverslip and the well system was then transferred to the plate bottom.

Seeding was performed in a BSL2+ biosafety cabinet. Expanded hESCs were rinsed with PBS and treated with Accutase for 15 min at room temperature. Cells were collected, spun down for 3 min at 200 × g, aspirated, resuspended at 3 million cells/ml in mTeSR Plus with 10 µM Y27632, and transferred to a pipetting reservoir. Using a multichannel pipette, 50 µl of cell suspension was added to 24 wells of a 96-well plate (CellTreat) for viral mixing. 50 µl of viral supernatant was added to each well

and mixed gently before transfer of the full 100 μ l to each well of the 24-well system for seeding. Cells were incubated for 1 hr in a tissue culture hood to form attachment to the Matrigel. Wells were then rinsed with DPBS with $\text{Ca}^{2+}/\text{Mg}^{2+}$ (Lonza), the well system was removed, and the plate received one final rinse in DPBS before addition of fresh mTeSR Plus with 10 μ M Y27632. 24 hr post-seed, media was changed to mTeSR Plus without Y27632.

Immunostaining

Live organoids were rinsed in DPBS, fixed for 1 hr at room temperature in 4% formaldehyde, and rinsed three times with PBS. Organoids were fixed between Day 1 (1 day of BMP4) treatment and Day 4 (4 days of BMP4 treatment) for time course analysis. All terminal morphologies were analyzed at Day 4. Because of organoid size, each primary and secondary antibody staining step was done at 4°C on a shaker set to 100 rpm for 48 hr under foil. Organoid morphologies were assayed with Alexa-647-conjugated NCAD antibody (CST 99377; RRID:AB_2800316) and Alexa-488-conjugated ECAD antibody (CST 3199; RRID:AB_10691457). ZO1 was stained with FITC-conjugated primary antibody (Invitrogen 33–9111; RRID:AB_2533148). TFAP2A was stained with primary antibody (DSHB 3B5; RRID:AB_2313948) and secondary antibody Invitrogen A31571 (RRID:AB_162542). OCT4 was stained with primary antibody CST 2840 (RRID:AB_2167691) and secondary antibody Invitrogen A31573 (RRID:AB_2536183).

Epifluorescence imaging of fixed and live samples

Epifluorescence microscopy was performed on a Zeiss AxioObserver Z1 inverted microscope with Zeiss 10x and 20x NA 1.3 plan apo objectives. Images were acquired with an Orca-Flash 4.0 CMOS camera (Hamamatsu). LED light was filtered using Zeiss filter sets 43 HE DsRed, 46 HE YFP, 47 HE CFP, 49 DAPI, and 50 Cy5.

For live imaging, a live imaging lid with a CO_2 nozzle was constructed for a 10-cm plate. Cells were imaged with 37°C incubation and 5% CO_2 . Transduction efficiency was examined at 48 hr post-seed with live epifluorescence microscopy in phase and 47 HE CFP channels. For live timelapses of actin, organoids were incubated in media containing 50 nM SiR-actin for 24 hr, then imaged for the indicated timeframes after BMP4 addition.

Confocal imaging of fixed samples

Confocal microscopy was performed on a Zeiss LSM 980 with Airyscan using a Zeiss 10x NA 0.45 objective. Z-stacks were performed through whole organoids. Single slices through the middle of each organoid are presented in figures.

scRNA-seq library preparation

Neural tube organoids were collected at Days 2 and 4 (after 48 or 96 hr of BMP4 treatment, respectively) for dissociation. Day 4 organoids perturbed with different guides were pooled for sequencing. Organoids were scraped off glass coverslips into a new 10 cm dish, diluted in 5 ml of PBS, collected, and spun down for 2 min at 200 \times g. PBS was then aspirated until there was 0.5 ml left in the tube, and cells were resuspended and transferred with a wide-bore pipette into a fresh 10 cm dish. Cells were then incubated in Accutase in a tissue culture hood for 20 min, then pipetted up and down with a narrow bore pipette to break up clumps. Single cells were spun down for 3 min at 200 \times g, aspirated, and resuspended at 1.1 million cells/ml in PBS + 0.04% BSA.

Cells were counted on the LUNA-FX7 Automated Cell Counter (Logos Biosystems) using fluorescence detection for viability with an acridine orange/propidium iodide stain (Part No. F23011). All samples had viability greater than 85%, with concentration ranges from 600 to 1500 cells/ μ l. After counting, all samples were loaded into Chip G per the user guide from 10x Genomics (Part No. CG000316). GEMs were formed targeting 3000–22,000 cells and reverse transcription completed immediately after. The *Feature cDNA Primers 3* (Part No. 2000289) were used to amplify cDNA from poly-adenylated mRNA and sgRNA containing either capture sequence 1 or capture sequence 2. Size selection was used to separate the amplified cDNA molecules for 3' Gene Expression and for CRISPR screening library construction. The amplified cDNA was verified via TapeStation (4200 TapeStation instrument, Agilent Technologies) using High Sensitivity D5000 tape and reagents (Part Nos. 5067-5592 and 5067-5593).

The amplified cDNA from poly-adenylated mRNA was fragmented, end repaired, and A-tailed followed by adaptor ligation, and PCR amplification with each sample receiving a unique set of dual indices (Part No. 1000215). The cDNA from sgRNA molecules was further amplified and the CRISPR Screening libraries were then generated by PCR amplification with each sample receiving a unique set of dual indices (Part No. PN-1000242).

Final libraries were diluted and ran using the High Sensitivity D5000 tape and reagents (Part No. 5067-5592 and 5067-5593) on the 4200 TapeStation (Agilent Technologies). Libraries were quantified via Kapa qPCR using the Complete Universal Kit (Part No. 07960140001, Roche Sequencing Solutions) and the CFX96 Touch Real-Time PCR Detection System (Bio-Rad Laboratories). Libraries were sequenced on an Illumina NovaSeq 6000 instrument using the parameters outlined in the user guide (Read1: 28 bp, i7 index: 10 bp, i5 index: 10 bp, Read2: 90 bp). After sequencing and demultiplexing, data are analyzed with Cell Ranger Count pipeline.

Quantification of transduction efficiency

Transduction efficiency analysis was performed on live epifluorescence microscopy of micropatterned stem cells, 48 hr after transduction and immediately before 3D cyst induction with Matrigel. Ilastik was trained to recognize the circular outline of each micropatterned colony in the phase channel and to return the center coordinates and diameters (d) of each colony. Circle parameters were then applied to the mCerulean channel in Python to extract mCerulean pixel values both from the colony and from a 2D background halo ($d + 10$ to $d + 35$ pixels). Colony pixels were categorized as mCerulean+ if they reached expression above the 95th percentile value in the background halo. Some micropatterns were located under the CO₂ adapter during live imaging and thus their transduction efficiency could not be measured.

For nuclear OCT4 knockdown analysis, nuclear centers were selected via DAPI stain in Fiji. Ten-pixel positions surrounding and including the nuclear center were extracted in Python from the OCT4 channel and summed to score OCT4 intensity. OCT4 values of each nucleus ($n > 600$ per micropatterned circle) were binned into histograms. An OCT4- nucleus was defined as having lower than the 5th percentile of nuclear OCT4 values in CFP- nuclei.

Organoid morphology analysis

Organoid morphology analysis was performed on epifluorescence microscopy images of Day 4 organoids using the Ilastik software platform. User-generated labels and epifluorescence were used to distinguish neural tube tissue (NCAD-positive) and non-neural tissue (ECAD-positive) through machine-learning pattern-based pixel classification. Morphological characteristics were extracted from the segmented objects, including area measurements. For organoid size quantification, adjacent NCAD- and ECAD-positive regions were summed to determine total organoid area. For ECAD/NCAD area, the former areas were divided.

scRNA-seq analysis of Day 2 and 4 organoids and Week 3 and 4 human embryos

After sequencing and demultiplexing, FASTQ files were run through the 10X Cell Ranger Count pipeline to align reads to the GRCh38-2020 reference genome, make guide calls according to capture sequencing, and produce a cell by gene count matrix.

For Day 2 and 4 organoids, Week 3 embryos, and Week 4 embryos (Zeng *et al.*, 2023), gene expression was analyzed in Python with Scanpy (v1.10.2). For each dataset, cells with too few or too many reads (potential doublets) were excluded from analysis based on manual cutoffs. All other cells were analyzed with SMD (Melton and Ramanathan, 2021) to find informative genes for clustering. Cells were then clustered using Scanpy's Louvain or Leiden algorithm in the space of the top 100–250 SMD genes (excluding ribosomal, mitochondrial, and cell cycle factors) with a clustering resolution of 0.2–0.5. In the case of Week 3 and 4 embryos, multiple rounds of clustering were performed to first identify non-ectodermal cell types and re-cluster ectodermal cell types only. In all cases, clusters were identified based on expression of canonical markers, including transcription factors. Cells were assigned to neural plate, neural plate border, and surface ectoderm for subsequent analysis. Raw reads of included cells were converted to transcripts per million (TPM) and log_{1p}-normalized prior to further analysis.

Mediolateral axis analysis of Day 2 data was performed on log_{1p}-normalized reads with Scanpy. First, principal component coordinates for each cell were calculated with `scanpy.tl.pca` using SciPy's ARPACK solver. Cells were color-coded along principal components 1 and 2 by their Louvain cluster identifications to find the neural-to-non-neural orientation along principal component 1. A nearest neighbors' distance matrix was then generated using `scanpy.pp.neighbors` with a local neighborhood size of 20. Diffusion pseudospace coordinates for each cell were calculated with `scanpy.tl.dpt`, using the least-neural cell on the principal component axis as the root cell.

For Day 4 organoids, guide calls and counts were merged with the cell by gene count matrix according to cell barcode in Python. Guide conditions were selected for analysis if at least 10 cells were sequenced from that guide condition (12 out of 18 non-scramble guides met this criteria). Knock-down efficacy of each guide condition was measured against a scramble guide control condition using an Anderson–Darling test (SciPy) with a significance cutoff of $p < 0.05$. This test was chosen for its use in determining if two distributions are statistically different. Gene expression of neural genes in each selected guide condition was compared to scramble control. Genes were defined as differentially expressed if they passed an Anderson–Darling with $p < 0.05$.

Motif enrichment analysis

Gene names that were strongly downregulated in *ZIC2*-perturbed organoids ($\log_2(\text{mean fold change relative to scramble control}) < -0.04$) were bulk-converted to ENSEMBL IDs using `g.Profiler`. Genomic regions (10 kb upstream of start site and 100 bp regions downstream of start site) were extracted using the Eukaryotic Promoter Database (EPD). Regions were analyzed with MEME-SEA for enrichment of transcription factor motifs relative to scrambled sequences. Enrichment scores of transcription factor families with multiple enriched motifs were combined for a final family enrichment score.

Acknowledgements

We thank Nicole Ramirez, Claire Reardon, Jeffery Nelson, Claire Maesner, Christian Daly, Nathan Weeks, and Zachary Niziolek at the Bauer Core Facility at Harvard University for performing single-cell RNA sequencing and assisting with FACS for cell line generation, and Doug Richardson at the Harvard Center for Biological Imaging for help with imaging. We thank Cassandra Extavour, Sean Megason, Jessica Whited, Vlad Denic, and members of the Ramanathan lab for scientific discussions and comments. This work was supported by NIH R01MH136014 (SR), NIH R01GM131105 (SR), and startup funds from Harvard University. REH was additionally funded by a National Science Foundation Graduate Research Fellowship.

Additional information

Competing interests

Roya E Huang, Giridhar M Anand, Heitor C Megale, Sharad Ramanathan: is an author on the following patent application, which contains aspects of this work: "Bioengineering and machine learning framework for complex tissue development". Application serial number PCT/US24/28838. The other authors declare that no competing interests exist.

Funding


Funder	Grant reference number	Author
National Institutes of Health	R01MH136014	Sharad Ramanathan
National Institutes of Health	R01GM131105	Sharad Ramanathan
U.S. National Science Foundation	Graduate Research Fellowship Program	Roya E Huang

The funders had no role in study design, data collection, and interpretation, or the decision to submit the work for publication.

Author contributions

Roya E Huang, Conceptualization, Resources, Data curation, Software, Formal analysis, Supervision, Funding acquisition, Validation, Investigation, Visualization, Methodology, Writing – original draft, Writing – review and editing; Giridhar M Anand, Conceptualization, Resources, Data curation, Software, Formal analysis, Supervision, Validation, Investigation, Visualization, Methodology, Writing – original draft, Writing – review and editing; Heitor C Megale, Investigation, Methodology; Jason Chen, Software, Formal analysis, Investigation, Visualization; Chudi Abraham-Igwe, Software, Investigation; Sharad Ramanathan, Conceptualization, Supervision, Funding acquisition, Writing – original draft, Project administration, Writing – review and editing

Author ORCIDs

Roya E Huang  <https://orcid.org/0000-0001-7267-4758>
 Giridhar M Anand  <https://orcid.org/0009-0002-0565-6642>
 Sharad Ramanathan  <https://orcid.org/0000-0001-9445-1248>

Peer review material

Reviewer #1 (Public review): <https://doi.org/10.7554/eLife.108224.3.sa1>
 Author response <https://doi.org/10.7554/eLife.108224.3.sa2>

Additional files**Supplementary files**

MDAR checklist

Data availability

Raw scRNA-seq data will remain unpublished to protect donor patient privacy, in accordance with Institutional Review Board (IRB) protocol and updated WiCell contract restrictions on publishing RNA sequences derived from human embryonic stem cells. Cell-by-gene count matrices from this paper are available at Figshare dataset [2026_HuangAnand](#). Code from this paper is available at GitHub repository [royahuang/2026_HuangAnand](#), copy archived at [Huang and Anand, 2026](#). Requests for detailed protocols will be fulfilled by corresponding authors Roya Huang (roya_huang@berkeley.edu) and Giridhar Anand (anand1g@mskcc.org). Requests for plasmids and cell lines will be fulfilled by the lead contact, Sharad Ramanathan (sharad@cgr.harvard.edu). Materials will be provided upon completion of a Material Transfer Agreement. Ex vivo scRNA-seq data from [Zeng et al., 2023](#), can be found at GEO accession number GSE155121.

The following dataset was generated:

Author(s)	Year	Dataset title	Dataset URL	Database and Identifier
Huang RE, Anand GM, Megale HC, Chen J, Abraham-Igwe C, Ramanathan S	2026	2026_HuangAnand	https://doi.org/10.6084/m9.figshare.31151509	figshare, 10.6084/m9.figshare.31151509

The following previously published dataset was used:

Author(s)	Year	Dataset title	Dataset URL	Database and Identifier
Liu Z, Zeng B, Zhong S, Wang X, Wu Q	2023	The single-cell and spatial transcriptional landscape of human development	https://www.ncbi.nlm.nih.gov/geo/query/acc.cgi?acc=GSE155121	NCBI Gene Expression Omnibus, GSE155121

References

[Aguilera-Castrejon A](#), [Oldak B](#), [Shani T](#), [Ghanem N](#), [Itzkovich C](#), [Slomovich S](#), [Tarazi S](#), [Bayerl J](#), [Chugueva V](#), [Ayyash M](#), [Ashoukhi S](#), [Sheban D](#), [Livnat N](#), [Lasman L](#), [Viukov S](#), [Zerbib M](#), [Addadi Y](#), [Rais Y](#), [Cheng S](#),

- Stelzer Y, et al. 2021. Ex utero mouse embryogenesis from pre-gastrulation to late organogenesis. *Nature* **593**:119–124. DOI: <https://doi.org/10.1038/s41586-021-03416-3>, PMID: 33731940
- Al-Jawahiri R**, Foroutan A, Kerkhof J, McConkey H, Levy M, Haghshenas S, Rooney K, Turner J, Shears D, Holder M, Lefroy H, Castle B, Reis LM, Semina EV, University of Washington Centre for Mendelian Genomics (UW-CMG), Lachlan K, Chandler K, Wright T, Clayton-Smith J, Hug FP, et al. 2022. SOX11 variants cause a neurodevelopmental disorder with infrequent ocular malformations and hypogonadotropic hypogonadism and with distinct DNA methylation profile. *Genetics in Medicine* **24**:1261–1273. DOI: <https://doi.org/10.1016/j.gim.2022.02.013>, PMID: 35341651
- al Yacoub N**, Romanowska M, Haritonova N, Foerster J. 2007. Optimized production and concentration of lentiviral vectors containing large inserts. *The Journal of Gene Medicine* **9**:579–584. DOI: <https://doi.org/10.1002/jgm.1052>, PMID: 17533614
- Anand GM**, Megale HC, Murphy SH, Weis T, Lin Z, He Y, Wang X, Liu J, Ramanathan S. 2023. Controlling organoid symmetry breaking uncovers an excitable system underlying human axial elongation. *Cell* **186**:497–512. DOI: <https://doi.org/10.1016/j.cell.2022.12.043>, PMID: 36657443
- Bondurand N**, Kobetz A, Pingault V, Lemort N, Encha-Razavi F, Couly G, Goerich DE, Wegner M, Abitbol M, Goossens M. 1998. Expression of the SOX10 gene during human development. *FEBS Letters* **432**:168–172. DOI: [https://doi.org/10.1016/s0014-5793\(98\)00843-6](https://doi.org/10.1016/s0014-5793(98)00843-6), PMID: 9720918
- Bonnard C**, Navaratnam N, Ghosh K, Chan PW, Tan TT, Pomp O, Ng AYJ, Tohari S, Changede R, Carling D, Venkatesh B, Altunoglu U, Kayserili H, Reversade B. 2020. A loss-of-function NUA2 mutation in humans causes anencephaly due to impaired Hippo-YAP signaling. *The Journal of Experimental Medicine* **217**:e20191561. DOI: <https://doi.org/10.1084/jem.20191561>, PMID: 32845958
- Britton G**, Heemskerk I, Hodge R, Qutub AA, Warmflash A. 2019. A novel self-organizing embryonic stem cell system reveals signaling logic underlying the patterning of human ectoderm. *Development* **146**:dev179093. DOI: <https://doi.org/10.1242/dev.179093>, PMID: 31519692
- Brown LY**, Dong W, Kantor B. 2020. An improved protocol for the production of lentiviral vectors. *STAR Protocols* **1**:100152. DOI: <https://doi.org/10.1016/j.xpro.2020.100152>, PMID: 33377046
- Corbin JG**, Rutlin M, Gaiano N, Fishell G. 2003. Combinatorial function of the homeodomain proteins Nkx2.1 and Gsh2 in ventral telencephalic patterning. *Development* **130**:4895–4906. DOI: <https://doi.org/10.1242/dev.00717>, PMID: 12930780
- Corsini NS**, Knoblich JA. 2022. Human organoids: New strategies and methods for analyzing human development and disease. *Cell* **185**:2756–2769. DOI: <https://doi.org/10.1016/j.cell.2022.06.051>, PMID: 35868278
- Debacker C**, Catala M, Labastie MC. 1999. Embryonic expression of the human GATA-3 gene. *Mechanisms of Development* **85**:183–187. DOI: [https://doi.org/10.1016/s0925-4773\(99\)00088-x](https://doi.org/10.1016/s0925-4773(99)00088-x), PMID: 10415360
- Dottori M**, Gross MK, Labosky P, Goulding M. 2001. The winged-helix transcription factor Foxd3 suppresses interneuron differentiation and promotes neural crest cell fate. *Development* **128**:4127–4138. DOI: <https://doi.org/10.1242/dev.128.21.4127>, PMID: 11684651
- Elms P**, Siggers P, Napper D, Greenfield A, Arkell R. 2003. Zic2 is required for neural crest formation and hindbrain patterning during mouse development. *Developmental Biology* **264**:391–406. DOI: <https://doi.org/10.1016/j.ydbio.2003.09.005>, PMID: 14651926
- Esk C**, Lindenhofer D, Haendeler S, Wester RA, Pflug F, Schroeder B, Bagley JA, Elling U, Zuber J, von Haeseler A, Knoblich JA. 2020. A human tissue screen identifies a regulator of ER secretion as a brain-size determinant. *Science* **370**:935–941. DOI: <https://doi.org/10.1126/science.abb5390>, PMID: 33122427
- Finkelshtein D**, Werman A, Novick D, Barak S, Rubinstein M. 2013. LDL receptor and its family members serve as the cellular receptors for vesicular stomatitis virus. *PNAS* **110**:7306–7311. DOI: <https://doi.org/10.1073/pnas.1214441110>, PMID: 23589850
- Fleck JS**, Jansen SMJ, Wollny D, Zenk F, Seimiya M, Jain A, Okamoto R, Santel M, He Z, Camp JG, Treutlein B. 2023. Inferring and perturbing cell fate regulomes in human brain organoids. *Nature* **621**:365–372. DOI: <https://doi.org/10.1038/s41586-022-05279-8>, PMID: 36198796
- Ha YJJ**, Nisal A, Tang I, Lee C, Jhamb I, Wallace C, Howarth R, Schroeder S, Vong KI, Meave N, Jiwani F, Barrows C, Lee S, Jiang N, Patel A, Bagga K, Banka N, Friedman L, Blanco FA, Yu S, et al. 2025. The contribution of de novo coding mutations to meningomyelocele. *Nature* **641**:419–426. DOI: <https://doi.org/10.1038/s41586-025-08676-x>, PMID: 40140573
- Hempel A**, Pagnamenta AT, Blyth M, Mansour S, McConnell V, Kou I, Ikegawa S, Tsurusaki Y, Matsumoto N, Lo-Castro A, Plessis G, Albrecht B, Battaglia A, Taylor JC, Howard MF, Keays D, Sohal AS, DDD Collaboration, Kühl SJ, Kini U, et al. 2016. Deletions and de novo mutations of SOX11 are associated with a neurodevelopmental disorder with features of Coffin-Siris syndrome. *Journal of Medical Genetics* **53**:152–162. DOI: <https://doi.org/10.1136/jmedgenet-2015-103393>, PMID: 26543203
- Hermesz E**, Mackem S, Mahon KA. 1996. Rpx: a novel anterior-restricted homeobox gene progressively activated in the prechordal plate, anterior neural plate and Rathke's pouch of the mouse embryo. *Development* **122**:41–52. DOI: <https://doi.org/10.1242/dev.122.1.41>, PMID: 8565852
- Hofbauer P**, Jahnel SM, Papai N, Giesshammer M, Deyett A, Schmidt C, Penc M, Tavernini K, Grdseloff N, Meledeth C, Ginistrelli LC, Ctorteka C, Šalic Š, Novatchkova M, Mendjan S. 2021. Cardioids reveal self-organizing principles of human cardiogenesis. *Cell* **184**:3299–3317. DOI: <https://doi.org/10.1016/j.cell.2021.04.034>, PMID: 34019794
- Hofer M**, Lutolf MP. 2021. Engineering organoids. *Nature Reviews. Materials* **6**:402–420. DOI: <https://doi.org/10.1038/s41578-021-00279-y>, PMID: 33623712

- Huang RE, Anand GM. 2026. 2026_HuangAnand. swh:1:rev:dd0c80ba3a29947a4e7f7d040f75d568f40936c6. Software Heritage. https://archive.softwareheritage.org/swh:1:dir:988ba56c140091a9908fc8322624d5948687eb85;origin=https://github.com/royahuang/2026_HuangAnand;visit=swh:1:snp:fe9442491e969bf16df9357b115d7e4ddb6453b;anchor=swh:1:rev:dd0c80ba3a29947a4e7f7d040f75d568f40936c6
- Huber A, Dijkstra C, Ernst M, Eissmann MF. 2023. Generation of gene-of-interest knockouts in murine organoids using CRISPR-Cas9. *STAR Protocols* **4**:102076. DOI: <https://doi.org/10.1016/j.xpro.2023.102076>, PMID: 36853714
- Ishida M, Cullup T, Boustred C, James C, Docker J, English C, Lench N, Copp AJ, Moore GE, Greene NDE, Stanier P, GOSgene. 2018. A targeted sequencing panel identifies rare damaging variants in multiple genes in the cranial neural tube defect, anencephaly. *Clinical Genetics* **93**:870–879. DOI: <https://doi.org/10.1111/cge.13189>, PMID: 29205322
- Jacobson AG. 1991. Experimental analyses of the shaping of the neural plate and tube. *American Zoologist* **31**:628–643. DOI: <https://doi.org/10.1093/icb/31.4.628>
- Justice MJ, Dhillon P. 2016. Using the mouse to model human disease: increasing validity and reproducibility. *Disease Models & Mechanisms* **9**:101–103. DOI: <https://doi.org/10.1242/dmm.024547>, PMID: 26839397
- Karfunkel P. 1974. The mechanisms of neural tube formation. *International Review of Cytology* **38**:245–271. DOI: [https://doi.org/10.1016/s0074-7696\(08\)60927-4](https://doi.org/10.1016/s0074-7696(08)60927-4), PMID: 4605295
- Karzbrun E, Khankhel AH, Megale HC, Glasauer SMK, Wyle Y, Britton G, Warmflash A, Kosik KS, Siggia ED, Shraiman BI, Streichan SJ. 2021. Human neural tube morphogenesis in vitro by geometric constraints. *Nature* **599**:268–272. DOI: <https://doi.org/10.1038/s41586-021-04026-9>, PMID: 34707290
- Laclef C, Hamard G, Demignon J, Souil E, Houbron C, Maire P. 2003. Altered myogenesis in Six1-deficient mice. *Development* **130**:2239–2252. DOI: <https://doi.org/10.1242/dev.00440>, PMID: 12668636
- Leask A, Byrne C, Fuchs E. 1991. Transcription factor AP2 and its role in epidermal-specific gene expression. *PNAS* **88**:7948–7952. DOI: <https://doi.org/10.1073/pnas.88.18.7948>, PMID: 1716766
- Lee JY, Lee HH. 2018. A new chemical complex can rapidly concentrate lentivirus and significantly enhance gene transduction. *Cytotechnology* **70**:193–201. DOI: <https://doi.org/10.1007/s10616-017-0133-0>, PMID: 28884364
- Li JY, Joyner AL. 2001. Otx2 and Gbx2 are required for refinement and not induction of mid-hindbrain gene expression. *Development* **128**:4979–4991. DOI: <https://doi.org/10.1242/dev.128.24.4979>, PMID: 11748135
- Li H, Zhang J, Chen S, Wang F, Zhang T, Niswander L. 2018. Genetic contribution of retinoid-related genes to neural tube defects. *Human Mutation* **39**:550–562. DOI: <https://doi.org/10.1002/humu.23397>, PMID: 29297599
- Li C, Fleck JS, Martins-Costa C, Burkard TR, Themann J, Stuempflen M, Peer AM, Vertesy Á, Littleboy JB, Esk C, Elling U, Kasprian G, Corsini NS, Treutlein B, Knoblich JA. 2023. Single-cell brain organoid screening identifies developmental defects in autism. *Nature* **621**:373–380. DOI: <https://doi.org/10.1038/s41586-023-06473-y>, PMID: 37704762
- Mandegar MA, Huebsch N, Frolov EB, Shin E, Truong A, Olvera MP, Chan AH, Miyaoka Y, Holmes K, Spencer CI, Judge LM, Gordon DE, Eskildsen TV, Villalta JE, Horlbeck MA, Gilbert LA, Krogan NJ, Sheikh SP, Weissman JS, Qi LS, et al. 2016. CRISPR interference efficiently induces specific and reversible gene silencing in human iPSCs. *Cell Stem Cell* **18**:541–553. DOI: <https://doi.org/10.1016/j.stem.2016.01.022>, PMID: 26971820
- McLarren KW, Litsiou A, Streit A. 2003. DLX5 positions the neural crest and preplacode region at the border of the neural plate. *Developmental Biology* **259**:34–47. DOI: [https://doi.org/10.1016/s0012-1606\(03\)00177-5](https://doi.org/10.1016/s0012-1606(03)00177-5), PMID: 12812786
- Melton S, Ramanathan S. 2021. Discovering a sparse set of pairwise discriminating features in high-dimensional data. *Bioinformatics* **37**:202–212. DOI: <https://doi.org/10.1093/bioinformatics/btaa690>, PMID: 32730566
- Menche C, Farin HF. 2021. Strategies for genetic manipulation of adult stem cell-derived organoids. *Experimental & Molecular Medicine* **53**:1483–1494. DOI: <https://doi.org/10.1038/s12276-021-00609-8>, PMID: 34663937
- Miao Y, Djeflal Y, De Simone A, Zhu K, Lee JG, Lu Z, Silberfeld A, Rao J, Tarazona OA, Mongera A, Rigoni P, Diaz-Cuadros M, Song LMS, Di Talia S, Pourquié O. 2023. Reconstruction and deconstruction of human somitogenesis in vitro. *Nature* **614**:500–508. DOI: <https://doi.org/10.1038/s41586-022-05655-4>, PMID: 36543321
- Nagai T, Aruga J, Minowa O, Sugimoto T, Ohno Y, Noda T, Mikoshiba K. 2000. Zic2 regulates the kinetics of neurulation. *PNAS* **97**:1618–1623. DOI: <https://doi.org/10.1073/pnas.97.4.1618>, PMID: 10677508
- Nakatsu T, Uwabe C, Shiota K. 2000. Neural tube closure in humans initiates at multiple sites: evidence from human embryos and implications for the pathogenesis of neural tube defects. *Anatomy and Embryology* **201**:455–466. DOI: <https://doi.org/10.1007/s004290050332>, PMID: 10909899
- Nikolopoulou E, Galea GL, Rolo A, Greene NDE, Copp AJ. 2017. Neural tube closure: cellular, molecular and biomechanical mechanisms. *Development* **144**:552–566. DOI: <https://doi.org/10.1242/dev.145904>, PMID: 28196803
- Nüsslein-Volhard C, Wieschaus E. 1980. Mutations affecting segment number and polarity in *Drosophila*. *Nature* **287**:795–801. DOI: <https://doi.org/10.1038/287795a0>, PMID: 6776413
- Nüsslein-Volhard C. 2012. The zebrafish issue of development. *Development* **139**:4099–4103. DOI: <https://doi.org/10.1242/dev.085217>, PMID: 23093421
- Oldak B, Wildschutz E, Bondarenko V, Comar M-Y, Zhao C, Aguilera-Castrejon A, Tarazi S, Viukov S, Pham TXA, Ashoukhi S, Lokshtanov D, Roncato F, Ariel E, Rose M, Livnat N, Shani T, Joubran C, Cohen R, Addadi Y, Chemla M, et al. 2023. Complete human day 14 post-implantation embryo models from naive ES cells. *Nature* **622**:562–573. DOI: <https://doi.org/10.1038/s41586-023-06604-5>, PMID: 37673118

- Oliver G**, Mailhos A, Wehr R, Copeland NG, Jenkins NA, Gruss P. 1995. Six3, a murine homologue of the sine oculis gene, demarcates the most anterior border of the developing neural plate and is expressed during eye development. *Development* **121**:4045–4055. DOI: <https://doi.org/10.1242/dev.121.12.4045>, PMID: 8575305
- O’Rahilly R**, Müller F. 2002. The two sites of fusion of the neural folds and the two neuropores in the human embryo. *Teratology* **65**:162–170. DOI: <https://doi.org/10.1002/tera.10007>, PMID: 11948562
- Ortmann D**, Vallier L. 2017. Variability of human pluripotent stem cell lines. *Current Opinion in Genetics & Development* **46**:179–185. DOI: <https://doi.org/10.1016/j.gde.2017.07.004>, PMID: 28843810
- Püschel AW**, Westerfield M, Dressler GR. 1992. Comparative analysis of Pax-2 protein distributions during neurulation in mice and zebrafish. *Mechanisms of Development* **38**:197–208. DOI: [https://doi.org/10.1016/0925-4773\(92\)90053-m](https://doi.org/10.1016/0925-4773(92)90053-m), PMID: 1457381
- Replogle JM**, Norman TM, Xu A, Hussmann JA, Chen J, Cogan JZ, Meer EJ, Terry JM, Riordan DP, Srinivas N, Fiddes IT, Arthur JG, Alvarado LJ, Pfeiffer KA, Mikkelsen TS, Weissman JS, Adamson B. 2020. Combinatorial single-cell CRISPR screens by direct guide RNA capture and targeted sequencing. *Nature Biotechnology* **38**:954–961. DOI: <https://doi.org/10.1038/s41587-020-0470-y>, PMID: 32231336
- Replogle JM**, Saunders RA, Pogson AN, Hussmann JA, Lenail A, Guna A, Mascibroda L, Wagner EJ, Adelman K, Lithwick-Yanai G, Iremadze N, Oberstrass F, Lipson D, Bonnar JL, Jost M, Norman TM, Weissman JS. 2022. Mapping information-rich genotype-phenotype landscapes with genome-scale Perturb-seq. *Cell* **185**:2559–2575. DOI: <https://doi.org/10.1016/j.cell.2022.05.013>, PMID: 35688146
- Roellig D**, Tan-Cabugao J, Esaian S, Bronner ME. 2017. Dynamic transcriptional signature and cell fate analysis reveals plasticity of individual neural plate border cells. *eLife* **6**:e21620. DOI: <https://doi.org/10.7554/eLife.21620>, PMID: 28355135
- Sanaki-Matsumiya M**, Kageyama R. 2022. Time-lapse bioluminescence imaging of Hes7 expression in vitro and ex vivo. *Methods in Molecular Biology* **2525**:321–332. DOI: https://doi.org/10.1007/978-1-0716-2473-9_25, PMID: 35836080
- Schelshorn DW**, Schneider A, Kuschinsky W, Weber D, Krüger C, Dittgen T, Bürgers HF, Sabouri F, Gassler N, Bach A, Maurer MH. 2009. Expression of hemoglobin in rodent neurons. *Journal of Cerebral Blood Flow and Metabolism* **29**:585–595. DOI: <https://doi.org/10.1038/jcbfm.2008.152>, PMID: 19116637
- Singh N**, Kumble Bhat V, Tiwari A, Kodaganur SG, Tontanahal SJ, Sarda A, Malini KV, Kumar A. 2017. A homozygous mutation in TRIM36 causes autosomal recessive anencephaly in an Indian family. *Human Molecular Genetics* **26**:1104–1114. DOI: <https://doi.org/10.1093/hmg/ddx020>, PMID: 28087737
- Skarnes WC**, Rosen B, West AP, Koutsourakis M, Bushell W, Iyer V, Mujica AO, Thomas M, Harrow J, Cox T, Jackson D, Severin J, Biggs P, Fu J, Nefedov M, de Jong PJ, Stewart AF, Bradley A. 2011. A conditional knockout resource for the genome-wide study of mouse gene function. *Nature* **474**:337–342. DOI: <https://doi.org/10.1038/nature10163>, PMID: 21677750
- Smith JL**, Schoenwolf GC. 1997. Neurulation: coming to closure. *Trends in Neurosciences* **20**:510–517. DOI: [https://doi.org/10.1016/s0166-2236\(97\)01121-1](https://doi.org/10.1016/s0166-2236(97)01121-1), PMID: 9364665
- Sock E**, Rettig SD, Enderich J, Bösl MR, Tamm ER, Wegner M. 2004. Gene targeting reveals a widespread role for the high-mobility-group transcription factor Sox11 in tissue remodeling. *Molecular and Cellular Biology* **24**:6635–6644. DOI: <https://doi.org/10.1128/MCB.24.15.6635-6644.2004>, PMID: 15254231
- Sun D**, Evans L, Perrone F, Sokleva V, Lim K, Rezakhani S, Lutolf M, Zilbauer M, Rawlins EL. 2021. A functional genetic toolbox for human tissue-derived organoids. *eLife* **10**:e67886. DOI: <https://doi.org/10.7554/eLife.67886>, PMID: 34612202
- Takagi T**, Moribe H, Kondoh H, Higashi Y. 1998. DeltaEF1, a zinc finger and homeodomain transcription factor, is required for skeleton patterning in multiple lineages. *Development* **125**:21–31. DOI: <https://doi.org/10.1242/dev.125.1.21>, PMID: 9389660
- Torres M**, Gómez-Pardo E, Gruss P. 1996. Pax2 contributes to inner ear patterning and optic nerve trajectory. *Development* **122**:3381–3391. DOI: <https://doi.org/10.1242/dev.122.11.3381>, PMID: 8951055
- Valcourt JR**, Huang RE, Kundu S, Venkatasubramanian D, Kingston RE, Ramanathan S. 2021. Modulating mesendoderm competence during human germ layer differentiation. *Cell Reports* **37**:109990. DOI: <https://doi.org/10.1016/j.celrep.2021.109990>, PMID: 34758327
- Van de Putte T**, Maruhashi M, Francis A, Nelles L, Kondoh H, Huylebroeck D, Higashi Y. 2003. Mice lacking ZFX1B, the gene that codes for Smad-interacting protein-1, reveal a role for multiple neural crest cell defects in the etiology of Hirschsprung disease-mental retardation syndrome. *American Journal of Human Genetics* **72**:465–470. DOI: <https://doi.org/10.1086/346092>, PMID: 12522767
- van der Valk WH**, van Beelen ESA, Steinhart MR, Nist-Lund C, Osorio D, de Groot JCMJ, Sun L, van Benthem PPG, Koehler KR, Locher H. 2023. A single-cell level comparison of human inner ear organoids with the human cochlea and vestibular organs. *Cell Reports* **42**:112623. DOI: <https://doi.org/10.1016/j.celrep.2023.112623>, PMID: 37289589
- Virtual Human Embryo**. 2026. Virtual Human Embryo. <https://www.ehd.org/virtual-human-embryo> [Accessed June 16, 2026].
- Walther C**, Gruss P. 1991. Pax-6, a murine paired box gene, is expressed in the developing CNS. *Development* **113**:1435–1449. DOI: <https://doi.org/10.1242/dev.113.4.1435>, PMID: 1687460
- Xu Y**, Baldassare M, Fisher P, Rathbun G, Oltz EM, Lynchopoulos GD, Jessell TM, Alt FW. 1993. LH-2: a LIM/homeodomain gene expressed in developing lymphocytes and neural cells. *PNAS* **90**:227–231. DOI: <https://doi.org/10.1073/pnas.90.1.227>, PMID: 7678338

- Xue L**, Cai JY, Ma J, Huang Z, Guo MX, Fu LZ, Shi YB, Li WX. 2013. Global expression profiling reveals genetic programs underlying the developmental divergence between mouse and human embryogenesis. *BMC Genomics* **14**:568. DOI: <https://doi.org/10.1186/1471-2164-14-568>, PMID: 23961710
- Xue X**, Liu Y, Fu J. 2025. Bioengineering embryo models. *Nature Reviews Bioengineering* **3**:11–29. DOI: <https://doi.org/10.1038/s44222-024-00241-x>
- Yaman YI**, Ramanathan S. 2023. Controlling human organoid symmetry breaking reveals signaling gradients drive segmentation clock waves. *Cell* **186**:513–527.. DOI: <https://doi.org/10.1016/j.cell.2022.12.042>, PMID: 36657441
- Yamanaka Y**, Hamidi S, Yoshioka-Kobayashi K, Munira S, Sunadome K, Zhang Y, Kurokawa Y, Ericsson R, Mieda A, Thompson JL, Kerwin J, Lisgo S, Yamamoto T, Moris N, Martinez-Arias A, Tsujimura T, Alev C. 2023. Reconstituting human somitogenesis in vitro. *Nature* **614**:509–520. DOI: <https://doi.org/10.1038/s41586-022-05649-2>, PMID: 36543322
- Yuan W**, Chen J, Cao Y, Yang L, Shen L, Bian Q, Bin S, Li P, Cao J, Fang H, Gu H, Li H. 2018. Comparative analysis and optimization of protocols for producing recombinant lentivirus carrying the anti-Her2 chimeric antigen receptor gene. *The Journal of Gene Medicine* **20**:e3027. DOI: <https://doi.org/10.1002/jgm.3027>, PMID: 29851200
- Zeng B**, Liu Z, Lu Y, Zhong S, Qin S, Huang L, Zeng Y, Li Z, Dong H, Shi Y, Yang J, Dai Y, Ma Q, Sun L, Bian L, Han D, Chen Y, Qiu X, Wang W, Marín O, et al. 2023. The single-cell and spatial transcriptional landscape of human gastrulation and early brain development. *Cell Stem Cell* **30**:851–866. DOI: <https://doi.org/10.1016/j.stem.2023.04.016>, PMID: 37192616